High-Frequency Limit of the Inverse Scattering Problem: Asymptotic Convergence from Inverse Helmholtz to Inverse Liouville[*]

Shi Chen[†], Zhiyan Ding[‡], Qin Li[†], and Leonardo Zepeda-Núñez[¶]

Abstract. We investigate the asymptotic relation between the inverse problems relying on the Helmholtz equation and the radiative transfer equation (RTE) as physical models in the high-frequency limit. In particular, we evaluate the asymptotic convergence of a generalized version of the inverse scattering problem based on the Helmholtz equation, to the inverse scattering problem of the Liouville equation (a simplified version of RTE). The two inverse problems are connected through the Wigner transform that translates the wave-type description on the physical space to the kinetic-type description on the phase space, and the Husimi transform that models data localized both in location and direction. The finding suggests that impinging tightly concentrated monochromatic beams can indeed provide stable reconstruction of the medium, asymptotically in the high-frequency regime. This fact stands in contrast with the unstable reconstruction for the classical inverse scattering problem when the probing signals are plane waves.

Key words. inverse scattering, Wigner transform, Husimi transform, high-frequency limit

MSC codes. 65N21, 78A46, 81S30

DOI. 10.1137/22M147075X

1. Introduction. The wave-particle duality of light has been one of the greatest enigmas in the natural sciences, dating back to Euclid's treatise in light, *Catoptrics* (280 B.C.) and spanning more than two millennia. In a nutshell, light can be either described as an electromagnetic (EM) wave governed by the Maxwell's equations, or as a stream of particles, called photons, governed by the radiative transport equation (RTE).

Although the advent of quantum mechanics at the onset of the last century partially solved the riddle, due to computational considerations, light continues to be modeled either

[†]Department of Mathematics, University of Wisconsin-Madison, Madison, WI 53706 USA (schen636@wisc.edu, https://simonchenthu.github.io/, qinli@math.wisc.edu, https://people.math.wisc.edu/~qinli/).

[‡]Department of Mathematics, University of Wisconsin-Madison, Madison, WI 53706 USA. Current address: Department of Mathematics, University of California-Berkeley, Berkeley CA 94720 USA (zding.m@math.berkeley.edu, https://math.berkeley.edu/zding.m/).

[¶]Department of Mathematics, University of Wisconsin-Madison, Madison, WI 53706 USA. Current address:: Google Research, Mountain View, CA 94043 USA (lzepedanunez@google.com, https://people.math.wisc.edu/~lzepeda/).

as a particle or as a wave depending on the target application. Among those applications, inverse problems are perhaps the ones that have gained the most attention in the last decades, which in return have fueled many breakthroughs in telecommunications [53, 54], radar [17], biomedical imaging [4, 45], and, more recently, in chip manufacturing [30]. In this context, inverse problems can be roughly described as reconstructing unknown parameters within a domain of interest by data comprised of observations on its boundary.

Unfortunately, the properties of the inverse problems are highly dependent on the specific modeling of the underlying physical phenomena, even though, in principle, they share the same microscopic description. In particular, the stability of the inverse problem, i.e., how sensitive is the reconstruction of the unknown parameter to perturbations in the data, is surprisingly disparate [14, 36], thus creating an important gap between the wave and particle descriptions, which we seek to bridge in this paper. We point out that understanding this gap is not only of theoretical importance, it would also play an important role in designing new reconstruction algorithms with improved stability applicable to a broader set of wave-based inverse problems, which are ubiquitous in science [39, 43, 49] and engineering [2, 19, 40].

For simplicity, we consider a time-harmonic wave-like description governed by the Helmholtz equation, which can be derived from the time-harmonic Maxwell's equations after some simplifications. Alternatively, the Helmholtz equation can also be obtained by computing the Fourier transform of the constant-density acoustic wave equation at frequency k, which is given by[1]

$$(1.1) \qquad \left(\Delta + k^2 n\right) u(x) = 0 \,,$$

where u is the wave field and $n(x)$ is the refractive index of the medium. We point out that even if this is a simplified model, it retains the core difficulty of more complex physics.

We also consider a particle-like description governed by the Liouville equation, which is a simplified RTE, given by

$$(1.2) \qquad v \cdot \nabla_x f - \nabla_x n \cdot \nabla_v f = 0,$$

where $f(x,v)$ is the distribution of photon particles and n is still the refractive index. The Liouville equation describes the trajectories of photons via its characteristics: $\dot{x} = v$ and $\dot{v} = -\nabla_x n$. For simplicity we neglect the photon interactions which are usually encoded by the collision operator.

Following the wave and photon descriptions, we define the forward problem as calculating either the wavefield, or the photon distribution from the refractive index by solving either the Helmholtz or the Liouville equations. The wave-particle duality, when translated to mathematical language, corresponds to the fact that the solutions obtained by the Helmholtz and Liouville equations are asymptotically close when $k \to \infty$; see [3].

For the sake of conciseness, we consider a simplified inverse problem consisting of reconstructing an unknown environment within a domain of interest by probing it with tightly concentrated monochromatic beams originated from the boundary of the domain, in which the response of the unknown medium to the impinging beam is measured at its boundary. This measurement is performed by a measurement operator that is model specific and it will play an important role in what follows. For simplicity, we consider the full aperture regime,

---

[1]The domain of definition, source, and boundary conditions will be specified in section 2.

i.e., we can probe the medium from any direction, and we sample its impulse response in all possible directions. When the beam is modeled as a wave, i.e., using the Helmholtz equation as a forward model, this process can be considered as a *generalized* version of the inverse scattering wave problem (which we, for the sake of clarity, just refer to as the *generalized Helmholtz scattering problem*. When the beam is modeled as a flux of photons, i.e., using the Liouville equation as a forward model, this process is often referred to as the *optical tomography problem*, but we will refer to as the *Liouville scattering problem* in this manuscript.

Although the two different formulations seek to solve the same underlying physical problem, our understanding of the two inverse problems seems to suggest different stability properties. The traditional inverse scattering problem, using either near-field or far-field data is ill-posed: small perturbations in the measurements usually lead to large deviations in the reconstructions [20, 28]. Thus, sophisticated algorithms [5, 9, 16, 22, 23, 33, 41] have been designed to artificially stabilize the process by appropriately restricting the class of possible unknown environments, usually in the form of band-limited environments. Conversely, the inverse Liouville equation is well-conditioned: a small perturbation is reflected by a small error in the reconstruction [38].

Thus the observation that the stability for both problems is different seems to be at odds with the fact that the Liouville equation and the Helmholtz equation are asymptotically close in the high-frequency regime. Fortunately, as what we will see, this somewhat contradictory property stems from the inability of *traditional* formulations of the inverse problems to agree in the high-frequency limit. When the measurement operators are accordingly adjusted, we show that the new formulations, which we call the generalized inverse scattering, are equivalent in the limit as $k \to \infty$, producing a stable inverse problem. The convergence from the Helmholtz equation to the Liouville equation is conducted through the Wigner transform [3, 25, 44], and the convergence of the measuring operators is achieved through the Husimi transform [8]. Both convergences are obtained asymptotically in the $k \to \infty$ limit. This convergence allows us to conclude the following:

The inverse Liouville scattering problem is asymptotically equivalent to the generalized inverse Helmholtz scattering problem in the high-frequency regime.

The current manuscript is dedicated to formulating the statement above in a mathematically precise manner, while providing extensive numerical evidence supporting the statement.

On the mathematical level, the current paper carries the following important features:

- The result connects the two seemingly distinct inverse problems, and suggests that in the high-frequency regime, probing an unknown object with a single frequency is already enough for its reconstruction, with properly prepared data in the generalized inverse scattering setting. This partially answers the stability question regarding the inverse scattering.
- The result can be viewed as the counterpart of the asymptotic multiscale study conducted in the forward setting. In particular, the semiclassical limit is a theory that connects quantum mechanical and the classical mechanical description: the proposed formulation for the inverse scattering problem can be regarded as taking the (semi)classical limit in the inverse setting, and thus the work carries conceptual merits.

This is in line with [14, 36]. See also [32] for a different setting.

These mathematical understandings also naturally bring numerical and practical benefits. The new inverse wave scattering formulation coupled with PDE-constrained optimization seems to be empirically less prone to cycle-skipping, i.e., convergence to spurious local minima [52], than its standard counterparts [9, 51], thus potentially opening the way to more robust algorithmic pipelines for inverse problems.

We point out that even though this current study is motivated by the wave-particle duality of light, the current results are also applicable to other oscillatory phenomena; see [14] for a discussion on inverse Schrödinger problem in the classical limit.

Organization. In section 2, we briefly review the Helmholtz equation and present the corresponding inverse problem that fits the particular experimental setup that allows passing the system to the $k \to \infty$ limit. In section 3, we discuss the limiting Liouville equation and the inverse Liouville scattering problem, by conducting the Wigner and Husimi transforms. The connections between the two inverse problems will thus be immediate. Finally, we present our numerical evidence that justifies the convergence in section 4 and we showcase the stability of the inverse problem in section 5.

2. Experimental setup and inverse problem formulation. Suppose we use tightly concentrated monochromatic beams, or laser beams, to probe the medium. Each beam impinges in the area of interest, thus producing a scattered field which is then measured by directional receivers[2] placed on a manifold around the domain of interest. The data, which are used to reconstruct the optical properties of the medium, is the intensity captured by each receiver for each incoming beam. Thus, the data are indexed by the position and direction of the impinging beam, and the location and direction of the receivers.

In this section, we set up the experiment and provide the mathematical formulation, using both the wave and the particle forms for the forward model. This prepares us to link the two problems in section 3.

2.1. Helmholtz equation and inverse wave scattering problem. The Helmholtz equation is a model equation for time-harmonic wave propagation. After some approximations, both the constant-density acoustic wave equation and the Maxwell equations for the EM waves can be recast through the Fourier transform in t, into the Helmholtz equation. It writes as

$$(2.1) \qquad \Delta u^k + k^2 n(x) u^k = S^k(x).$$

In the equation, u^k is the wavefield, with the superscript, $k > 0$ represents the wave number (that carries the frequency information, and thus in the paper we use the two words interchangeably). $n(x)$ is a complex-valued refractive index having nonnegative imaginary part, $\text{Im}(n(x)) \geq 0$, reflecting the heterogeneity of the medium. We assume $n(x)$ is the constant one in all $\mathbb{R}^d$ except in a convex bounded open set $\Omega \subset \mathbb{R}^d$, meaning $\text{supp}(n-1) \subset \Omega$. In order to streamline the notation, we let $\Omega = B_1$, the ball with radius 1 centered around the origin. The right-hand side $S^k(x)$ is the source term, which is wavenumber dependent.

The classical setup for the scattering problem is to probe the medium with an incident wavefield $u^{i,k}$ that triggers the response from the medium. Noting that the total field, which satisfies (2.1), is the sum of the incident and the scattered wavefields, we can write

---

[2]Experimentally, this is often achieved by placing a collimator before the receiver, and changing the orientation of the collimator.

$$u^k = u^{i,k} + u^{s,k},$$

and derive the equation for the scattered wavefield $u^{s,k}$. Suppose the incident wave is designed so that it absorbs all the external source information,

$$(2.2) \qquad \Delta u^{i,k} + k^2 u^{i,k} = S^k(x),$$

then by simply subtracting it from (2.1), we have the equation for $u^{s,k}$:

$$(2.3) \qquad \begin{aligned} \Delta u^{s,k} + k^2 n(x) u^{s,k} &= k^2(1 - n(x)) u^{i,k}, \quad x \in \mathbb{R}^d, \\ \frac{\partial u^{s,k}}{\partial r} - \mathrm{i} k u^{s,k} &= \mathcal{O}(r^{-(d+1)/2}) \text{ as } r = |x| \to \infty. \end{aligned}$$

In this equation, we can view the incident wave $u^{i,k}$ impinging in the perturbation $n-1$ as the source term for $u^{s,k}$. Clearly, this source term $k^2(1 - n(x)) u^{i,k}$ is zero outside B_1, the support of $n-1$. The Sommerfeld radiation condition is imposed at infinity to ensure the uniqueness for $u^{s,k}$.

When $d = 3$, a typical approach is to set $S(x) = \delta_y$, a point Dirac delta, then the solution $u^{i,k}$ to (2.2) becomes the fundamental solution to the homogeneous Helmholtz equation in $\mathbb{R}^3$,

$$\Phi(x; y) = -\frac{1}{4\pi} \frac{\exp(ik|x - y|)}{|x - y|}, \quad x, y \in \mathbb{R}^3, x \neq y,$$

for any given y. We can clearly observe that the function is radially symmetric centered in y thus it is often termed a spherical wave. If $|y| \gg |x|$, i.e., y is far away from the origin, we have the far-field regime, in which the fundamental solution is approximately a plane wave: $\Phi(x; y) \approx -\frac{e^{ik|y|}}{4\pi|y|} \exp(-ik\hat{y} \cdot x)$.

In this case, however, instead of using the Dirac delta, we handcraft a specially designed source term, which will be crucial for the rescaling proposed in this article. In particular, we choose $S_{\mathrm{H}}^k(x)$ to be the following:

$$(2.4) \qquad S_{\mathrm{H}}^k(x; x_s, v_s) = -k^{\frac{3+d}{2}} S_{v_s}(k(x - x_s)), \quad x \in \mathbb{R}^d,$$

where the subscript H stands for Helmholtz, and

$$(2.5) \qquad S_{v_s}(x) = C(\sigma, d) \exp\left(-\sigma^2 \frac{|x|^2}{2} + \mathrm{i} v_s \cdot x\right).$$

Here $C(\sigma, d)$ is the normalization constant $C(\sigma, d) = \sqrt{2}\left(\frac{\sigma}{\sqrt{\pi}}\right)^{\frac{d+1}{2}}$.

Physically this source term can be understood as the source generating a tight beam being shone onto the medium from the location x_s in the direction of v_s. The profile of this tight beam, or "laser beam," is a Gaussian centered around the lightup location x_s and the width of the Gaussian is characterized by $(k\sigma)^{-1}$. With σ fixed, as $k \to \infty$, the beam is more and more concentrated.

Following the explanation above we incorporate the source term in (2.4) into (2.1)–(2.2), to probe the medium from the positions, x_s, in the direction of v_s, that are physically pertinent. In particular, we let $(x_s, v_s) \in \Gamma_-$ where

$$\Gamma_{\pm} = \{(x, v) \in \partial B_1 \times \mathbb{S}^{d-1} : \pm v \cdot \nu(x) > 0\},$$

in which $\nu(x)$ denotes the outer-normal direction at $x \in \partial B_1$. This means the laser beams shine from the boundary of B_1 in the direction v pointing inward the interior of the domain.

From (2.4) we can observe that as $k \to \infty$, the laser beam becomes increasingly concentrated. In particular, in the $k \to \infty$ limit, the incident wave $u^{i,k}$ becomes a ray, propagating through a straight line.[3]

As usual in inverse problems (in particular, in nonintrusive experimental setups), we take measurements of u^k near the boundary ∂B_1. To take such a measurement we design a family of test functions of the form

$$(2.6) \qquad \phi_v^k(x) = k^{d/4} \chi\left(\sqrt{k}x\right) e^{-ikv \cdot x},$$

where $\chi : \mathbb{R}^d \to \mathbb{R}$ is a smooth radially symmetric function that vanishes as $|x| \to \infty$.

We define the measurement of u^k as its Husimi transform

$$(2.7) \qquad H^k u^k(x, v) = \left(\frac{k}{2\pi}\right)^d \left|u^k * \phi_v^k\right|^2 \qquad \text{for } (x, v) \in \Gamma_+.$$

The measurement then consists of the intensity of the field that convolves with the test function. This measurement is conducted only on the boundary, and only in the directions pointing outside the domain.

This measurement has a clear physical interpretation: it measures the intensity of the wavefield at location x propagating in direction v, using χ as the impulse response of the receiver, or test function.

One typical choice for the family of test functions is to set χ as a Gaussian (normalized in the L^2 norm)

$$(2.8) \qquad \chi(x) = \left(\frac{1}{\pi}\right)^{d/4} \exp\left(-\frac{|x|^2}{2}\right).$$

It is straightforward to see that as $k \to \infty$, the test function ϕ_v^k concentrates around zero due to the $\sqrt{k}$ scaling. As such, the measurement $u^k * \phi_v^k$ at a location x_s only takes the value of u^k in a very small neighborhood around x_s.

Remark 2.1. We note that the choice of χ in (2.8) is not essential. We use this specific form to make the calculation explicit, as it will be shown in Proposition 3.4. Other forms of χ would also work well as long as the corresponding $G^k = W^k[\phi_0^k]$ converges to a Dirac delta when $k \to \infty$, as it will be explained in Remark 3.5.

Forward Map: now we have all the elements to define the forward map. For any $(x_s, v_s) \in \Gamma_-$, we shine a laser beam onto B_1 according to the format in (2.4), then the solution to the Helmholtz equation (2.1), u^k, is tested by $\phi_v^k(x)$ and evaluated on Γ_+:

$$(2.9) \qquad \Lambda_n^k : \quad S_H^k(x; x_s, v_s) \to H^k u^k(x_r, v_r)|_{\Gamma_+}.$$

As a consequence, the dataset generated by this forward map is the collection of:

$$(2.10) \qquad \mathcal{D}^k[n] = \left\{\left(S_H^k(x; x_s, v_s), \Lambda_n^k[S_H^k](x_r, v_r)\right) : (x_s, v_s) \in \Gamma_-, (x_r, v_r) \in \Gamma_+\right\}.$$

---

[3]The incoming ray propagates in a straight line due to the assumption that the background is constant. Otherwise, the ray would bend if a smooth nonconstant background is considered.

We now formulate the generalized inverse scattering problem as

$$(2.11) \qquad \textit{to reconstruct n using the information in } \mathcal{D}^k[n].$$

2.1.1. Traditional inverse scattering problem. Given that we use a nonstandard formulation of the inverse scattering problem, we will stress a couple of similarities and differences between the generalized and classical inverse scattering problems.

In particular, the form of the forward map introduced in our setting differs from the classical one, where the incident wave is typically a plane wave, meaning $u^{i,k}(x; v_s) = \exp(ikv_s \cdot x)$, where $v_s \in \mathcal{S}^{d-1}$: see [31].

So the forward map is given by the far-field map, $\widetilde{\Lambda}_n^k$,

$$\widetilde{\Lambda}_n^k : u^{i,k}(x; v_s) \to u^{\infty,k}(\hat{x}; v_s),$$

where $u^{\infty,k} : \mathcal{S}^{d-1} \to \mathbb{C}$ is defined as

$$u^{\infty,k}(\hat{x}; v_s) = \lim_{r \to \infty} r u^{s,k}(r\hat{x}; v_s) \exp(-ikr)|_{\hat{x} \in \mathcal{S}^{k-1}} \quad \forall \hat{x} \in \mathcal{S}^{d-1}$$

with $u^{s,k}$ being the solution of (2.3), where we leverage that $u^{i,k}(x; v_s)$ satisfies (2.2) with $S = 0$. Therefore, in this setting, the data set induced by the forward map is defined as

$$\widetilde{\mathcal{D}}^k[n] = \left\{ \left(u^{i,k}(x; v_s), \widetilde{\Lambda}_n^k \left[u^{i,k} \right] (\hat{x}) \right) : v_s \in \mathcal{S}^{d-1}, \hat{x} \in \mathcal{S}^{d-1} \right\}.$$

The well-posedness and stability of the inverse scattering problem in this context has been studied in [28, Theorem 1.2].

The differences from the classical inverse scattering formulation is twofold: (i) we use a richer set of probing functions, instead of using incident waves that are directionally localized (as plane waves) or whose sources are localized (as Green's functions), we use tight beams that combine these two properties, and (ii) instead of measuring the scattered wavefield on a manifold around the domain of interest, we multiply it with a set of directional filters localized on the same manifold, and we compute its intensity. We should emphasize that this difference is significant. Taking the plane wave as the probing wave, as an example, it is only the direction of the incoming wave that can be tuned, and this composes 2 dimensions of degrees of freedom in 3 dimensions with $v_s \in \mathcal{S}^{d-1}$. The way our source term is designed automatically carries 4 dimensions of degrees of freedom with $(x_s, v_s) \in \Gamma_-$. Similarly, the way data get taken also expands the degrees of freedom the measuring operator can access. It is a widely accepted fact that more data lead to more stable reconstruction. This will be indeed demonstrated in the later sections.

Remark 2.2. We note that even though the conventional inverse scattering problem has been shown to be ill-conditioned, a couple of strategies have been introduced in the literature to stabilize the problem. The most prominent strategy is to add the phase information (microlocally) [7, 18, 46]. At the first look, the Husimi data (2.7) also extracts the phase information, by integrating the scattered wave with an oscillatory test function (2.6) that is localized in position and direction. In very simple cases, we can even show that the two sets

of information are equivalent. For example, suppose the wavefield is of the simple form of $u^k(x) = A(x)e^{\mathrm{i}kp\cdot v}$ with $p \in \mathbb{S}^{d-1}$ and $A(x) \geq 0$ for all $x \in \mathbb{R}^d$. Then in the limit $k \to \infty$, we can fully recover $u^k(x)$, both the amplitude and the phase, on the boundary ∂B_1 using the Husimi data (2.7)

$$\lim_{k\to\infty} H^k u^k(x, v) = |A(x)|^2 \delta(v - p) \quad \forall (x, v) \in \partial B_1 \times \mathbb{S}^{d-1}.$$

However, in general cases, we are not aware of results that translate Husimi data to the phase data. Indeed, according to [1, 26, 27], this might be a very complicated phase retrieval problem that is beyond the scope of the current paper.

Remark 2.3. Another strategy to stabilize the inverse scattering problem is to transform the Helmholtz equation back to the time domain, and solve the inverse acoustic wave problem, with either full or partial data available for all time $T \geq 0$. In various settings [6, 29, 47, 55], it is proved that the time-domain data are sufficient to reconstruct the medium. The wave equation and Helmholtz equation are Fourier transforms of each other in time. Roughly speaking, the temporal data collected on the boundary translate to the boundary information for all frequencies k. As such, the temporal data have wideband information instead of being monochromatic, and thus are expected to be more stable. In our setting, though we require $k \gg 1$, we still use monochromatic information, and thus the data do not directly translate. We should note, however, that though the time-domain data are expected to be more informative in theory, in practice, however, especially within the optimization-based reconstruction algorithm framework, the typical ℓ^2 misfit loss function results in an extremely nonlinear problem that often leads to cycle skipping, and convergence to spurious, nonphysical, local minima. The numerical problem is usually attenuated by using the time/frequency duality and localizing the frequency content of the data, which is then processed in a hierarchical fashion [16, 41]. These are beyond the focus of the paper.

2.2. High-frequency limit and inverse Liouville scattering problem. The Liouville equation is a well-studied classical model for describing particle propagation. Any system with a large number of identical particles can be described by the Liouville equation, or its variants, which is often written as

(2.12)
$$v \cdot \nabla_x f + \frac{1}{2}\nabla_x n \cdot \nabla_v f = S_{\mathrm{L}}(x, v),$$

where $f(x, v)$ characterizes the number of particles on the phase space (x, v). Following the characteristics, we see that the particles follow Newton's second law:

$$\dot{x} = v, \quad \dot{v} = \frac{1}{2}\nabla_x n.$$

As usual in classical mechanics, we can define the Hamiltonian for each particle to be

$$H(x(t), v(t)) = \frac{1}{2}|v(t)|^2 - \frac{1}{2}n(x(t)),$$

which is preserved along the characteristics of the particles, i.e., $\frac{\mathrm{d}H}{\mathrm{d}t} = 0$.

We use (2.12) to describe photon propagation, and use the same setup as that in section 2.1. The source term $S_{\mathrm{L}}(x, v)$ on the right-hand side of (2.12) describes how laser beams are shone into the medium, and takes the form of

$$(2.13) \qquad S_{\mathrm{L}}(x, v; x_s, v_s) = \phi(x - x_s)\psi(v - v_s) \quad \text{with} \quad (x_s, v_s) \in \Gamma_-,$$

where both $\phi : \mathbb{R}^d \to \mathbb{R}$ and $\psi : \mathbb{R}^d \to \mathbb{R}$ are radially symmetric smooth functions that concentrate at the origin. By setting $(x_s, v_s) \in \Gamma_-$, we have the laser beam shining from the boundary ∂B_1 inward to the domain. The concentration of the beam is determined by ϕ and ψ in physical- and velocity-space, respectively.

Similarly to the previous section, we take the measurements of the light intensity at the boundary pointing outside of the domain. To do so, we set the test function $\zeta(x, v)$ and the measurements would be its convolution with the solution to (2.12):

$$(2.14) \qquad Lf(x, v) = f * \zeta(x, v).$$

The physical setup is clear. Imaging ζ a blob centers around $(x, v) = (0, 0)$, then $Lf(x_r, v_r)$ essentially represents a measuring equipment that takes in light intensity concentrated around (x_r, v_r) with the concentration determined by the size of the blob. The specific format of ζ will be specified in section 3.

Forward map: we define the forward map in a similar fashion as in section 2.1. For any $(x_s, v_s) \in \Gamma_-$, we solve (2.12) with S_{L} defined in (2.13), and test the solution on $\zeta(x, v)$ evaluated on Γ_+:

$$\Lambda_n : \quad S_{\mathrm{L}}(x, v; x_s, v_s) \to Lf(x_r, v_r)|_{\Gamma_+}.$$

As a consequence, the dataset generated by this forward map is the collection of

$$(2.15) \qquad \mathcal{D}[n] = \{(S_{\mathrm{L}}(x, v; x_s, v_s), \Lambda_n[S_{\mathrm{L}}](x_r, v_r)) : (x_s, v_s) \in \Gamma_-, (x_r, v_r) \in \Gamma_+\}.$$

While the forward problem is to compute and construct this $\mathcal{D}[n]$ for any given n, the inverse problem amounts to inferring n using the information in $\mathcal{D}[n]$.

3. Relation between the two problems in the high-frequency regime. In this section we discuss the connection between the forward maps for the wave- and particle-like descriptions introduced in the section above. We start introducing the Wigner transform, and we use it to present the equivalence of the two descriptions for the forward maps in the high-frequency regime. Then we introduce the Husimi transform to take the limit of the measuring operator, and this is used to show the equivalence of the two inverse problems. Finally, we briefly introduce the stability of the inverse Liouville problem.

3.1. High-frequency limit of the forward problem. We first present their connection in the forward setting. We discuss the derivation of the Liouville equation as the limiting equation for the Helmholtz. This process is typically called taking the "classical"-limit, to reflect the passage from quantum mechanics to classical mechanics by linking the Schrödinger equation to the Liouville equation in the small $\hbar$ regime.

Among the multiple techniques to derive the classical limit we utilize the Wigner transform [3, 15, 25, 44]. Compared to other techniques, such as WKB expansion [24] and Gaussian beam expansion [34, 42, 48], the Wigner transform presents the equation on the phase space,

and avoids the emerging singularities during the evolution. Let u_1^k and u_2^k be two functions, then the corresponding Wigner transform is defined as

$$(3.1) \qquad W^k[u_1^k, u_2^k](x, v) = \frac{1}{(2\pi)^d} \int_{\mathbb{R}^d} e^{iv\cdot y} u_1^k\left(x - \frac{y}{2k}\right) \overline{u_2^k}\left(x + \frac{y}{2k}\right) dy.$$

Here $\overline{u_2^k}$ is the complex conjugate of u_2^k. We furthermore abbreviate $W^k[u_1^k, u_2^k]$ to be $W^k[u^k]$.

The Wigner transform $W^k[u^k]$ is defined on the phase space, is always real valued, and the moments in v of $W^k[u^k]$ carry interesting physical meanings. In particular, the first moment recovers the energy density $\mathcal{E}^k$,

$$(3.2) \qquad \mathcal{E}^k(x) = \int_{\mathbb{R}^d} W^k[u^k](x, v)dv = \left|u^k(x)\right|^2,$$

and its second moment expresses the energy flux $\mathcal{F}^k$,

$$(3.3) \qquad \mathcal{F}^k(x) = \int_{\mathbb{R}^d} v W^k[u^k](x, v)dv = \frac{1}{k}\text{Im}\left(\overline{u^k(x)}\nabla_x u^k(x)\right).$$

Most importantly, if u^k solves the Helmholtz equation (2.1), one can show that $W^k[u^k]$ solves an equation in the form of the radiative transfer equation, and in the $k \to \infty$ limit, this degenerates to the Liouville equation (2.12). In what follows we seek to make this statement more precise by defining the functional space and an appropriate metric.

Letting $\lambda > 0$, we define X_λ a space that contains all scalar real valued functions defined on the phase space $\mathbb{R}^3 \times \mathbb{R}^3$,

$$(3.4) \qquad X_\lambda = \left\{\phi(x, y) \ \middle|\middle| \ \int_{\mathbb{R}^3} \sup_{x \in \mathbb{R}^3} (1 + |x| + |\xi|)^{1+\lambda}|\hat{\phi}(x, \xi)|d\xi < \infty\right\}$$

with associated norm given by

$$\|\phi\|_{X_\lambda} = \int_{\mathbb{R}^3} \sup_{x \in \mathbb{R}^3} (1 + |x| + |\xi|)^{1+\lambda}|\hat{\phi}(x, \xi)|d\xi,$$

where $\hat{\phi}(x, \xi) = \frac{1}{(2\pi)^d} \int_{\mathbb{R}^d} \phi(x, y)e^{-i\xi\cdot y}dy$ is the Fourier transform in velocity space. Now we cite a result from [8, Theorems 3.11, 3.12].

Theorem 3.1. *Let $n(x)$ be a $C^2(\mathbb{R}^d; \mathbb{R}_+)$ function that satisfies certain conditions (see Remark 3.2). Let u^k be the solution to (2.1) with radiation conditions, where the source term S_H^k is defined in (2.4). Then the Wigner transform of u^k, denoted by $f^k(x, v) = W^k[u^k](x, v)$, solves*

$$(3.5) \qquad v \cdot \nabla_x f^k + \frac{1}{2}\mathcal{L}_n^k[f^k] = -\frac{1}{k}\text{Im}\left(W^k[u^k, S^k]\right), \quad (x, v) \in \mathbb{R}^{2d},$$

with the operator $\mathcal{L}_n^k$ defined as

$$(3.6) \qquad \mathcal{L}_n^k[f^k] := \frac{i}{(2\pi)^d} \int_{\mathbb{R}^{2d}} \delta^k[n](x, y)f^k(x, p)e^{iy(v-p)} \, dy \, dp.$$

Here $\delta^k[n](x,y) = k\left[n\left(x + \frac{y}{2k}\right) - n\left(x - \frac{y}{2k}\right)\right]$. Furthermore, when $k \to \infty$, f^k converges in the weak-$\star$ sense to $f(x,v)$ in $(X_\lambda)^\star$, the solution to the Liouville equation (2.12) with the radiation condition $\lim_{|x|\to\infty} f(x,v) = 0$ for all $x \cdot v < 0$, and the source $S_\mathrm{L}(x,v)$ is

$$(3.7) \qquad S_\mathrm{L}(x,v) = (2\pi)^d \frac{\pi}{2} \delta(x - x_s) |\hat{S}_{v_s}(v)|^2 \delta\left(|v|^2 = n(x_s)\right).$$

Here $\hat{S}_{v_s}$ denotes the Fourier transform, and the delta function $\delta(|v|^2 = n(x_s)) \in \mathcal{D}'(\mathbb{R}^d)$ means

$$\langle \delta\left(|v|^2 = n(x_s)\right), g \rangle = \int_{|v|^2 = n(x_s)} g(v) dS_v \quad \forall g \in \mathcal{S}(\mathbb{R}^d).$$

Suppose S_v takes the form of (2.4), we can explicitly calculate its Fourier transform:

$$|\hat{S}_{v_s}(v)|^2 = C(\sigma, d)^2 \frac{1}{(2\pi)^d \sigma^{2d}} e^{-\frac{|v - v_s|^2}{\sigma^2}}.$$

Remark 3.2. The formal derivation of the limit is shown in Appendix A. To prove it rigorously, we refer to [8, Theorems 3.11, 3.12] and [12]. The conditions for a rigorous proof are rather complicated to obtain. However, we mention that if n is radially symmetric, i.e., $n(x) = n(|x|)$, the statement of the theorem holds true rigorously.

Theorem 3.1 suggests that the wave model and the particle model are asymptotically equivalent in the high-frequency regime. According to (3.7), the source term concentrates at (x_s, v_s), the source location and the source velocity, when $k \to \infty$. The concentration on x is already achieved by taking to the limit as $k \to \infty$, but the concentration profile in v still needs to be tuned by σ. A smaller σ results in a more concentrated source in this limiting regime. Letting $\sigma \to 0$, we have the source term S_L turning into

$$(3.8) \qquad \begin{aligned} (2\pi)^d \frac{\pi}{2} \delta(x - x_s) |\hat{S}_{v_s}(v)|^2 \delta(|v| = 1) &= \delta(x - x_s) \left(\frac{1}{\sigma\sqrt{\pi}}\right)^{d-1} e^{-\frac{|v - v_s|^2}{\sigma^2}} \delta(|v| = 1) \\ &\to \delta(x - x_s) \delta(v - v_s), \end{aligned}$$

where we used $n(x_s) = 1$, given that x_s is out of the domain of interest B_1.

In this specific limit, we have the explicit solution to the Liouville equation (2.12),

$$(3.9) \qquad f(x,v) = \delta_{(x(t;(x_s,v_s)),v(t;(x_s,v_s)))}, \quad k \to \infty,$$

where $(x(t;(x_s,v_s)), v(t;(x_s,v_s)))$ are the location and velocity of a particle at time t that starts off at (x_s, v_s), meaning $(x(0;(x_s,v_s)), v(0;(x_s,v_s))) = (x_s, v_s)$ and

$$(3.10) \qquad \begin{cases} \dfrac{\mathrm{d}x(t;(x_s,v_s))}{\mathrm{d}t} = v(t;(x_s,v_s)), \\ \dfrac{\mathrm{d}v(t;(x_s,v_s))}{\mathrm{d}t} = \dfrac{1}{2} \nabla_x n(x(t;(x_s,v_s))). \end{cases}$$

The formulation in (3.9) means in this limit, with $k \to \infty$ and $\sigma \ll 1$, the wave becomes a curved ray that follows the trajectory of the particle that is governed by Newton's laws. As a consequence, recall the definition of energy and energy flux in (3.2)–(3.3),

$$\lim_{\sigma \to 0} \lim_{k \to \infty} \mathcal{E}^k(x) = \mathbf{1}_{t>0} \delta_{x(t;(x_s,v_s))}, \quad \lim_{\sigma \to 0} \lim_{k \to \infty} \mathcal{F}^k(x) = \mathbf{1}_{t>0} \delta_{x(t;(x_s,v_s))} v(t;(x_s,v_s)),$$

suggesting that $\mathcal{E}^k$ and $\mathcal{F}^k$, respectively, show approximately the location and velocity of the trajectory.

3.2. High-frequency limit of the inverse problem. Earlier in the paper we linked the two forward problems. We now proceed to connect the two inverse problems by evaluating the convergence of the measurements. To do so, we first introduce Lemma 3.3 from [21, section 2.5] that connects the Husimi and Wigner transforms.

Lemma 3.3. *Assume $u \in L^2(\mathbb{R}^d; \mathbb{R})$, and let $H^k u$ be the Husimi transform defined in* (2.7) *with ϕ_v^k being the test function (defined in* (2.6)*). Denote $f^k = W^k[u]$ and $G^k = W^k[\phi_0^k]$, the Wigner transform of u^k and ϕ_0^k, respectively. Here $\phi_0^k = \phi_{v=0}^k$. Then*

$$(3.11) \qquad H^k u(x,v) = f^k * G^k(x,v) \quad \forall (x,v) \in \mathbb{R}^{2d}.$$

Proof. This theorem is a directly result of the Moyal identity

$$(3.12) \qquad (W^k[h_1], W^k[h_2])_{L^2(\mathbb{R}^{2d})} = \left(\frac{k}{2\pi}\right)^d |(h_1, h_2)_{L^2(\mathbb{R}^d)}|^2 \quad \forall h_1, h_2 \in L^2(\mathbb{R}^d; \mathbb{R}),$$

and the fact that

$$(3.13) \qquad W^k[\phi_v^k(x - \cdot)](y, p) = W^k[\phi_0^k](x - y, v - p).$$

Using (2.7), we have

$$
\begin{aligned}
H^k u(x,v) &= \left(\frac{k}{2\pi}\right)^d \left| u * \phi_v^k \right|^2 \\
&= \left(\frac{k}{2\pi}\right)^d \left| \left(u(\cdot), \phi_v^k(x - \cdot)\right)_{L^2(\mathbb{R}^d)} \right|^2 \\
&= \left(W^k[u], W^k[\phi_v^k(x - \cdot)]\right)_{L^2(\mathbb{R}^{2d})} \\
&= \left(W^k[u], W^k[\phi_0^k](x - \cdot, v - \cdot)\right)_{L^2(\mathbb{R}^{2d})} \\
&= f^k * G^k,
\end{aligned}
$$

where we use (3.12) in the third equality, (3.13) in the fourth equality, and the definitions of f^k and G^k in the last equality. ∎

This lemma connects the measurement of u^k with the measurement on the phase space. Testing u^k using the test function ϕ_0^k is translated to testing f^k using the test function G^k. This allows us to pass to the limit on the phase space. Combining with Theorem 3.1, we have the following proposition.

Proposition 3.4. *Let the assumption in Theorem* 3.1 *hold true. Denote $f^k = W^k[u^k]$ with u^k solving the Helmholtz equation* (2.1) *with the source term S_{H} defined in* (2.4)*, and denote f the solution to the Liouville equation* (2.12) *with source term S_{L} defined in* (3.7)*. If χ takes the form of* (2.8)*, so that G^k takes the form of*

$$(3.14) \qquad G^k(x,v) = \left(\frac{k}{\pi}\right)^d \exp\left(-k\left(|x|^2 + |v|^2\right)\right),$$

as $k \to \infty$, we have

$$f^k * G^k(x, v) \to f(x, v)$$

weak-$\star$ in $(X_\lambda)^\star$.

Proof. Given the form of G^k in (3.14), for any $\phi \in X_\lambda$, as $k \to \infty$,

$$G^k * \phi(x, v) \longrightarrow \phi(x, v) \quad \text{in} \quad X_\lambda.$$

Thus,

$$\lim_{k \to \infty} \int_{\mathbb{R}^3 \times \mathbb{R}^3} \left(f^k * G^k(x, v) \right) \phi(x, v) \mathrm{d}x \, \mathrm{d}v = \lim_{k \to \infty} \int_{\mathbb{R}^3 \times \mathbb{R}^3} f^k(x, v) \left(G^k * \phi(x, v) \right) \mathrm{d}x \, \mathrm{d}v$$

$$= \lim_{k \to \infty} \int_{\mathbb{R}^3 \times \mathbb{R}^3} f^k(x, v) \phi(x, v) \mathrm{d}x \, \mathrm{d}v$$

$$= \int_{\mathbb{R}^3 \times \mathbb{R}^3} f(x, v) \phi(x, v) \mathrm{d}x \, \mathrm{d}v,$$

where we use $\| f^k \|_{(X_\lambda)^*}$ being bounded in the second equality, and $f^k \to f$ in the weak-$\star$ sense in the last equality. ∎

Remark 3.5. We note that the statement of the proposition indeed uses the explicit form of χ as defined in (2.8), but the use only lies in the fact that $G^k * \phi(x, v) \longrightarrow \phi(x, v)$ in the high frequency limit. Other forms of χ works equally well as long as this G^k serves as a delta measure when $k \to \infty$.

Theorem 3.6. *Let the assumptions in Theorem 3.1 and Lemma 3.3 hold true, then*

$$\lim_{k \to \infty} H^k u^k(x, v) = \lim_{k \to \infty} f^k * G^k(x, v) \xrightarrow[\text{weak}-\star]{} f(x, v)$$

in $(X_\lambda)^*$. Furthermore, if $H^k u^k$ and f are continuous, then each element in $\mathcal{D}^k[n]$ has a limit in $\mathcal{D}[n]$. More specifically:

$$(3.15) \qquad (S_{\mathrm{H}}^k(x; x_s, v_s), \Lambda_n^k[S_{\mathrm{H}}^k](x_r, v_r)) \to (S_{\mathrm{L}}(x, v; x_s, v_s), \Lambda_n[S_{\mathrm{L}}](x_r, v_r)),$$

where S_{L} takes the form of (3.7), and $\Lambda_n[S_{\mathrm{L}}](x_r, v_r) = f(x_r, v_r)$. In particular, if $\sigma \to 0$,

$$(3.16) \qquad \Lambda_n[S_{\mathrm{L}}](x_r, v_r) = f * \delta_{(\vec{0}, \vec{0})}|_{\Gamma_+} = f(x_r, v_r)|_{\Gamma_+} = \delta(x - x_{r_s})\delta(v - v_{r_s})$$

with (x_{r_s}, v_{r_s}) being the outgoing location and velocity when the photon particle leaves the domain, namely,

$$(3.17) \qquad\qquad x_{r_s} = x(T; (x_s, v_s)), \quad v_{r_s} = v(T; (x_s, v_s)),$$

where $T = \sup_{t \geq 0}\{t \mid |x(t; (x_s, v_s)) \in B_1\}$ and $\{x(t; (x_s, v_s)), v(t; (x_s, v_s))\}$ solves (3.10).

This theorem naturally links the two inverse problems. In the $k \to \infty$ limit, the two datasets (2.10), (2.15) are asymptotically close with $\zeta = \delta_{(\vec{0}, \vec{0})}(x, v)$ in (2.14). In the limit of $k \to \infty$ and $\sigma \to 0$, the dataset (2.10) is asymptotically approximately equivalent to

$$(3.18) \qquad \mathcal{D}^\infty[n] = \{((x_s, v_s), (x_r, v_r)) : (x_s, v_s) \in \Gamma_-, \ (x_r, v_r) \text{ from } (3.17)\}.$$

3.3. Stability of Liouville inverse problem. In this section, we consider the stability of the Liouville inverse problem. In particular, we focus on the stability of (3.18). We will show that when n is close enough to 1, D_n^∞ almost contains the information of the X-ray transforms of $n(x)$ and $\nabla_x n(x)$, while the inverse of the X-ray transform is a well-posed inverse problem.

We first introduce the X-ray transform. Define

$$TS^{d-1} = \left\{ (x, v) \mid \mid x \in \mathbb{R}^d, \, v \in \mathcal{S}^{d-1}, \, \langle v, x \rangle = 0 \right\}.$$

Assuming that $n(x)$ is continuous, we introduce the X-ray transform P, which maps $n(x), \nabla_x n(x)$ into functions $Pn \in C(TS^{d-1}, \mathbb{R})$ and $P(\nabla_x n) \in C(TS^{d-1}, \mathbb{R}^d)$, such that

$$Pn(v, x) = \int_{-\infty}^{\infty} n(tv + x) \mathrm{d}t, \quad P(\nabla_x n)(v, x) = \int_{-\infty}^{\infty} \nabla_x n(tv + x) \mathrm{d}t.$$

To connect D_n^∞ with the X-ray transform, we define a projection map $\mathcal{P} : \partial B_1 \times \mathcal{S}^{d-1} \to \mathbb{R}^d \times \mathcal{S}^{d-1}$,

$$\mathcal{P}((x, v)) = (x - \langle x, v \rangle v, v),$$

that projects x to the plane with normal vector v. We also define the in-out map $\mathcal{L} : \Gamma_- \to \Gamma_+$ corresponding to (3.17):

$$\mathcal{L}((x_s, v_s)) = (x_r, v_r).$$

Remark 3.7. We remark that the in-out map may not be well-defined for arbitrarily given n. Suppose $n(x) \geq c_0$ for all $x \in \mathbb{R}^d$ and some $c_0 > 0$, then according to the conservation of the Hamiltonian

(3.19) $$H(x, v) = \frac{1}{2}|v|^2 - \frac{1}{2}n(x) = \frac{1}{2} - \frac{1}{2} = 0,$$

the velocity of the particle satisfies

$$|v(t)| = \sqrt{n(x(t))} \geq \sqrt{c_0} > 0$$

for all time $t \geq 0$. This by no means suggests the nontrapping property, but it at least ensures that the potential is not a sink. In the general case, we do assume that n is nontrapping, so that any incoming particle can eventually be expelled out of the domain again, making the map $\mathcal{L}$ well-defined. Such a nontrapping condition is closely related to geodesic X-ray transforms, and we list references [18, 35, 46] for interested readers. In our numerical examples, we choose the media to be locally repulsive in the sense that

(3.20) $$n(x) + x \cdot \nabla n(x) \geq c_1 > 0 \quad \forall x \in \mathbb{R}^d.$$

Let $(x(t), v(t))$ be any particle trajectory that solves (3.10). Given (3.20), we obtain the inequality

(3.21) $$\frac{\mathrm{d}^2}{\mathrm{d}t^2}\left(\frac{1}{2}|x(t)|^2\right) = |v(t)|^2 + x(t) \cdot \frac{\mathrm{d}v}{\mathrm{d}t} = n(x(t)) + x(t) \cdot \nabla n(x(t)) \geq c_1 > 0.$$

In the last equality, we have used Equation (3.19). By making use of (3.21), the particle is nontrapped since $|x(t)| \geq t\sqrt{\frac{1}{2}c_0}$ for sufficiently large $s > 0$.

We note that $\mathcal{P}((x,v)) \in TS^{d-1}$ for any $(x,v) \in \partial B_1 \times \mathcal{S}^{d-1}$, and $\mathcal{P}|_{\Gamma_-} : \Gamma_- \to \mathbb{R}^d \times \mathcal{S}^{d-1}, \mathcal{P}|_{\Gamma_+} : \Gamma_+ \to \mathbb{R}^d \times \mathcal{S}^{d-1}$ are invertible. Now, we are ready to introduce the following approximation theorem [38, Theorem 4.1].

Theorem 3.8. *Assume*

$$\|\nabla n(x)\|_{L^\infty} \le \Delta, \quad \|\|Hn(x)\|_F\|_{L^\infty} \le \Delta$$

for some $\Delta > 0$, then for any $(v,x) \in TS^{d-1}$, we have

$$\left|(Pn(v,x), P(\nabla_x n)(v,x)) - \mathcal{P}|_{\Gamma_+} \circ \mathcal{L} \circ \left(\mathcal{P}|_{\Gamma_-}\right)^{-1}(v,x)\right| \le C\Delta^2,$$

where $C > 0$ is a constant that only depends on d.

According to Theorem 3.8, if n is almost a constant (close enough to 1), then we can use the data set to recover the X-ray transform of $n, \nabla n(x)$. Thus, we can separate (3.18) into two inverse problems

$$\mathcal{D}^\infty[n] \Longrightarrow (Pn(v,x), P(\nabla_x n)(v,x)) \Longrightarrow n(x),$$

where the first one can be approximately calculated if n is an almost constant 1 and the second one is the inverse of the X-ray transform that is well-posed according to [37, Theorem 5.1].

4. Numerical experiments. In this section we provide numerical evidence showcasing the theory developed above. In particular, we would like to demonstrate that as k increases, the measurement taken on the solution to the Helmholtz equation through the Husimi transform converges to the pointwise evaluation of the solution to the Liouville equation, and that the data become more and more sensitive to the perturbation in media, making the inverse problem more and more stable.

We first summarize the numerical setup and unify the notations, and then present a class of numerical results.

4.1. Numerical setup. We set up our experiment in a two-dimensional domain (see Figure 1) that takes the form of

$$(4.1) \qquad \Delta u^k + k^2 n(x) u^k = -k^{\frac{5}{2}} S_{v_s}(k(x - x_s)), \quad x \in \mathbb{R}^2.$$

The Sommerfeld radiation condition is imposed at infinity as well. The source term is given by

$$(4.2) \qquad S_{v_s}(x) = \sqrt{2} \left(\frac{\sigma}{\sqrt{\pi}}\right)^{\frac{3}{2}} \exp\left(-\sigma^2 \frac{|x|^2}{2} + i v_s \cdot x\right)$$

for $(x_s, v_s) \in \Gamma_-$. We denote the solution to (4.1) by $u^k_{x_s, v_s}$ whenever the source center and the incident direction are relevant for the discussion. The Husimi transform defined in (2.7) takes the form

$$(4.3) \qquad H^k u^k(x_r, v_r) = \left(\frac{k}{2\pi}\right)^d \left|u^k * \phi^k_{v_r}(x_r)\right|^2$$

with $(x_r, v_r) \in \Gamma_+$. We let the refractive index $n(x)$ set to be $n(x) = 1 + q(x)$ with the support of the heterogeneity $q(x) \subset B(r)$. The measurement is taken on $\partial B(R)$ with $R > r$. See Figure 2 for an illustration of the configuration.
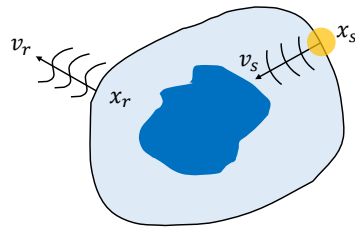
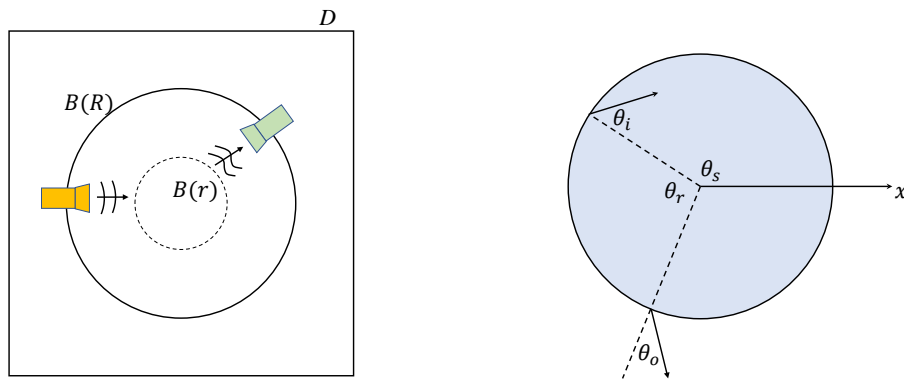**Figure 1.** *Illustration of the setup.*

Figure 2. *Left: Illustration of the setup for numerical experiments; right: sketch of the definition of the angles on the circle $\partial B(R)$ used to parameterize the data.*

Computationally we set the domain $D = [-L/2, L/2]^2$ with L significantly bigger than R, and choose the spatial mesh size $h = 1/N$ with N being an even integer. For simplicity of representation, we use the angles θ_s and θ_r to denote the center of the sources and the center of the receivers, respectively, and the angles θ_i and θ_o are used to denote the incident and outgoing direction of the sources and receivers, respectively, so that

$$
(4.4) \qquad \begin{aligned}
x_s &= (R\cos\theta_s, R\sin\theta_s), \\
v_s &= (-\cos(\theta_s + \theta_i), -\sin(\theta_s + \theta_i)),
\end{aligned}
$$

and

$$
(4.5) \qquad \begin{aligned}
x_r &= (R\cos(\theta_s + \theta_r), R\sin(\theta_s + \theta_r)), \\
v_r &= (\cos(\theta_s + \theta_r + \theta_o), \sin(\theta_s + \theta_r + \theta_o)).
\end{aligned}
$$

The angles θ_i and θ_o take values in $[0, 2\pi)$, whereas the angles θ_i and θ_o take values in $(-\frac{\pi}{2}, \frac{\pi}{2})$. An illustration of the angles can be found in Figure 2. Since the mapping between $(\theta_s, \theta_i, \theta_s, \theta_o)$ and the corresponding (x_s, v_s, x_r, v_r) is one-to-one, we present the quantities u^k and $H^k u^k$ on the θ coordinate system whenever there is no confusion.

The angles are discretized with step size $\Delta\theta$ and the angular grids are denoted by $\theta_s^j, \theta_r^j = j\Delta\theta$ for all $j = 0, \dots, 2\pi/\Delta\theta - 1$, and $\theta_i^j, \theta_o^j = -\frac{\pi}{2} + j\Delta\theta$ for all $j = 1, \dots, \pi/\Delta\theta - 1$.

To compare the Husimi transform of the solutions, we further define two quantities. The first quantity is the Husimi transform integrated in the outgoing direction,

$$(4.6) \qquad M_\mathrm{o}^k(x_\mathrm{s}, v_\mathrm{s}, x_\mathrm{r}) := \int_{\mathbb{S}_{x_\mathrm{r}}^+} H^k u_{x_\mathrm{s}, v_\mathrm{s}}^k(x_\mathrm{r}, v_\mathrm{r}) \mathrm{d}v_\mathrm{r} = \int_{-\pi/2}^{\pi/2} H^k u_{\theta_\mathrm{s}, \theta_\mathrm{i}}^k(\theta_\mathrm{r}, \theta_\mathrm{o}) \mathrm{d}\theta_\mathrm{o},$$

where $\mathbb{S}_{x_\mathrm{r}}^\pm = \{v \in \mathbb{S}^1 : \pm\nu(x_\mathrm{r}) \cdot v > 0\}$ and $\nu(x)$ is the unit outer normal vector at $x \in \partial\Omega$. Similarly, we also define the Husimi transform integrated along the outgoing boundary

$$(4.7) \quad M_\mathrm{r}^k(x_\mathrm{s}, v_\mathrm{i}, v_\mathrm{r}) := \int_{\partial\Omega_{v_\mathrm{r}}^+} H^k u_{x_\mathrm{s}, v_\mathrm{i}}^k(x_\mathrm{r}, v_\mathrm{r}) \mathrm{d}x_\mathrm{r} = \int_{(-\pi/2+\theta_\mathrm{or}, \pi/2+\theta_\mathrm{or})} H^k u_{\theta_\mathrm{s}, \theta_\mathrm{i}}^k(\theta_\mathrm{r}, \theta_\mathrm{or} - \theta_\mathrm{r}) \mathrm{d}\theta_\mathrm{r},$$

where we denote $\theta_\mathrm{or} = \theta_\mathrm{o} + \theta_\mathrm{r} \in [0, 2\pi)$, and define $\partial\Omega_{v_\mathrm{r}}^\pm = \{x \in \partial\Omega : \pm\nu(x) \cdot v_\mathrm{r} > 0\}$.

To solve the Helmholtz equation (4.1), we use the truncated kernel method [50], and solve for the Lippmann–Schwinger equation to obtain the scattered field $u^{\mathrm{s},k}$. This allows us to push for high-frequency without suffering from the numerical pollution that finite differences or finite elements methods often have. The scattered field is then combined with the incident field $u^{\mathrm{i},k}$ to yield u^k.

4.2. Numerical examples. In the first example, we set $L = 1$, $R = 0.3$, and $r = 0.25$. For the medium, we set the heterogeneity to be the radially symmetric smooth function

$$(4.8) \qquad q(x) = \begin{cases} A\exp\left(-\frac{1}{1-|x|^2/r^2}\right), & |x| < r, \\ 0, & \text{otherwise.} \end{cases}$$

Clearly, the support of $q(x)$ is contained in $B(r)$; see Figure 3. We note that with $-1 < A \leq 0$, the media is locally repulsive, and the incident wave is guaranteed to be expelled out of the domain. For the source term, we fix $\sigma = 2^{-5}$ in the following experiments. Noting that the medium $n(x)$ is radially symmetric, one can study the scattered data for a fixed source location. We choose $\theta_\mathrm{s} = \pi/4$; see Figure 3. For discretization, we choose spatial step size $h = 1/(2k)$ in the truncated kernel solver, and $\Delta\theta = \pi/30$ for the angular grids.
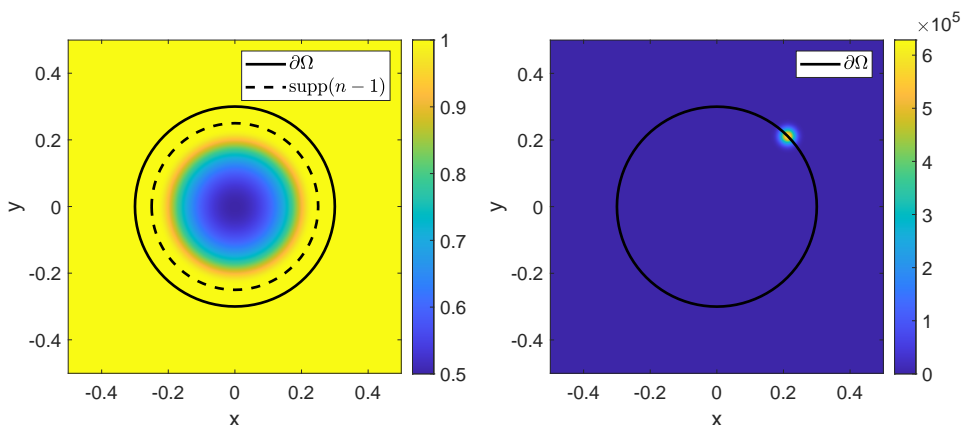

Figure 3. *The left plot illustrates the medium $n(x) = 1 + q(x)$ in (4.8) with $A = -0.5$. The right plot shows the amplitude of source $|S_{v_s}(k(x - x_s))|$ with $k = 2^{11}$, $\sigma = 2^{-5}$, and $\theta_\mathrm{s} = \pi/4$.*
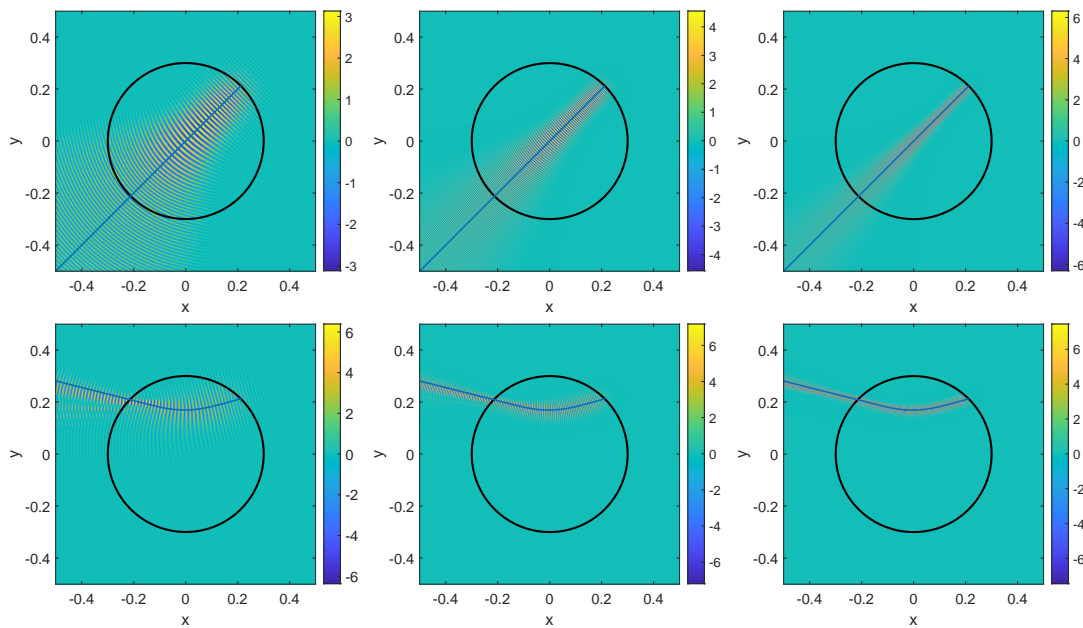
Figure 4. *The real part of u^k for $k = 2^9$ (left), $k = 2^{10}$ (middle), and $k = 2^{11}$ (right). The blue lines show the Liouville trajectory that solves* (3.10). *The medium* (4.8) *has amplitude $A = -0.5$. The incident direction $\theta_i = 0$ (upper) and $\theta_i = -\pi/6$ (lower).*

We first show the solution's behavior as k increases in Figure 4. As k increases, the solution converges to a narrow beam that follows the characteristic equation (3.10).

We compute the Husimi transform $H^k u^k$ for different k and we compare them with the trajectories of the Liouville equation. The results are shown in Figure 5, where we can observe that for a fixed θ_i, $H^k u^k$ converges to a delta function on the θ_r-θ_o plane, as k increases. This agrees with the statement in Theorem 3.1, especially (3.16).

We then compare the integrated Husimi transform defined in (4.6) and (4.7). In Figures 6 and 7, we demonstrate the convergence of M_o^k and M_r^k as k increases.

As k increases, the outgoing data become more and more sparse, and fewer and fewer detectors can receive outgoing light, leading to the sparser matrix presentation of Λ_n^k (see definition in (2.9). This is shown in Figure 8 for different k.

Finally we compare the change of Λ_n^k as n differs, for different k. Let $n_0(x) = 1$ as the background media whose corresponding map is denoted Λ_0^k, and by adjusting A we design a sequence of $n(x)$. We measure how the Frobenius norm $\|\Lambda_n^k - \Lambda_0^k\|_F$ changes with respect to $\|n - n_0\|_{L^\infty}$ for different k. As can be seen in Figure 9, as k increases, the slope of $\|\Lambda^k - \Lambda_0^k\|_F$ as $\|n - n_0\|_{L^\infty} \to 0$ increases. This confirms that bigger k sees more sensitivity of the data when n changes, hence the reconstruction is expected to be better for higher k.

5. Inversion algorithm. The inverse problem that we study in this article has a different setup from the conventional one. While the conventional setup has either the concentration in the incoming direction, or in the incoming source location, our experimental setup requires concentration in both direction and source location. Naturally we expect a better stability
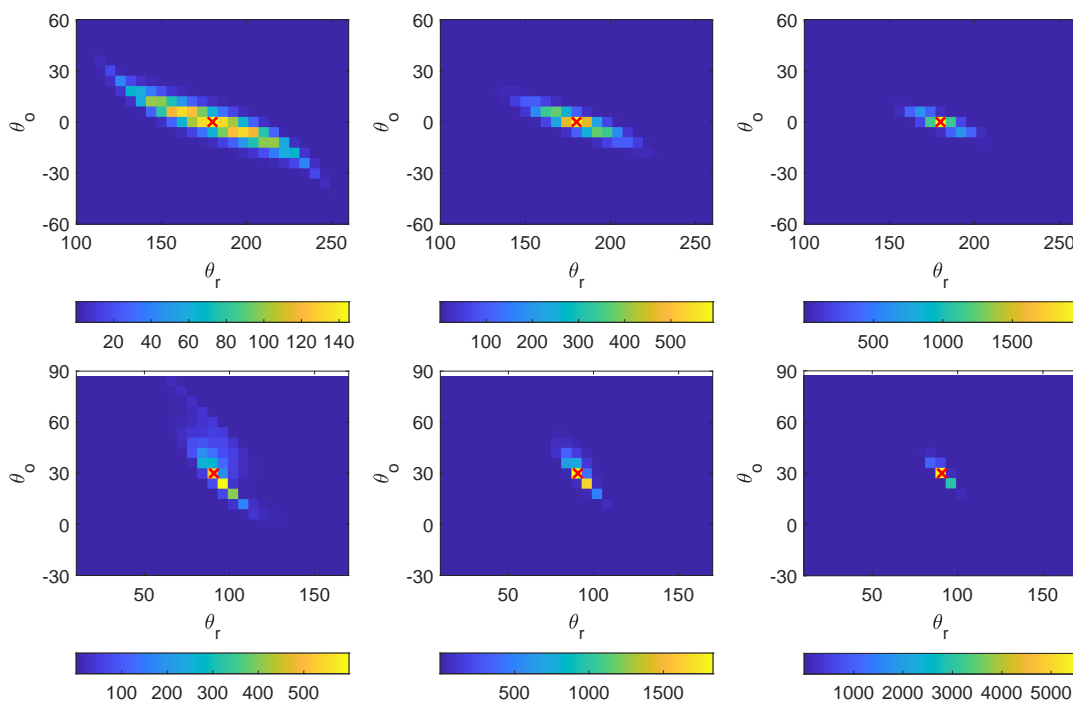
Figure 5. *The Husimi transform $H^k u^k$ for $k = 2^9$ (left), $k = 2^{10}$ (middle), and $k = 2^{11}$ (right). The upper row shows the results with $\theta_i = 0$, and the lower row shows the results with $\theta_i = -\pi/6$. The red crosses show the outgoing position and direction* (3.17) *of the Liouville trajectory. The medium* (4.8) *has amplitude $A = -0.5$.*
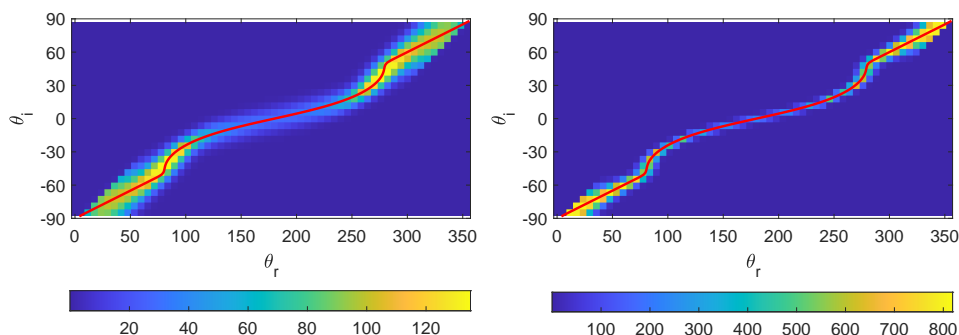

Figure 6. *The averaged Husimi transform M_o^k for $k = 2^9$ (left) and $k = 2^{11}$ (right). The red lines show the outgoing position* (3.17) *of the Liouville trajectory. The medium* (4.8) *has amplitude $A = -0.5$.*

in the reconstruction process, compared to the traditional formulation. In this section we showcase such stability.

Numerically the reconstruction process is formulated as a PDE-constrained minimization problem, where we seek to minimize the misfit between the data and the forward model,

$$(5.1) \qquad \min_n \left\| D - \mathcal{D}^k[n] \right\|^2_{L^2(\Gamma_- \times \Gamma_+)}$$
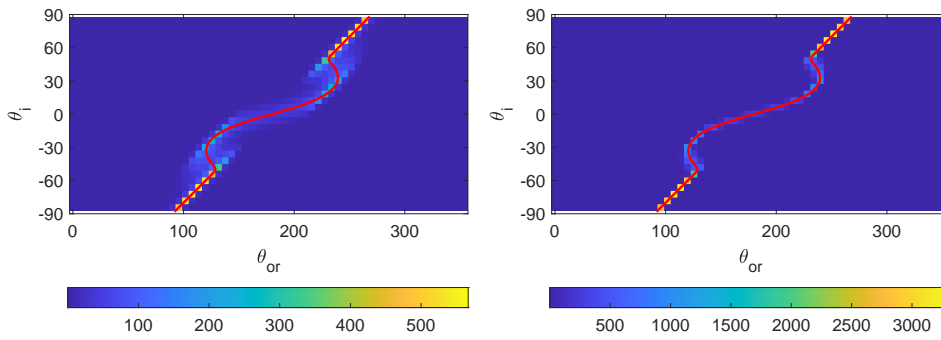
or, equivalently, in the discretized form

Figure 7. *The averaged Husimi transform M_r^k for $k = 2^9$ (left) and $k = 2^{11}$ (right). The red lines show the outgoing direction (3.17) of the Liouville trajectory. The medium (4.8) has amplitude $A = -0.5$.*
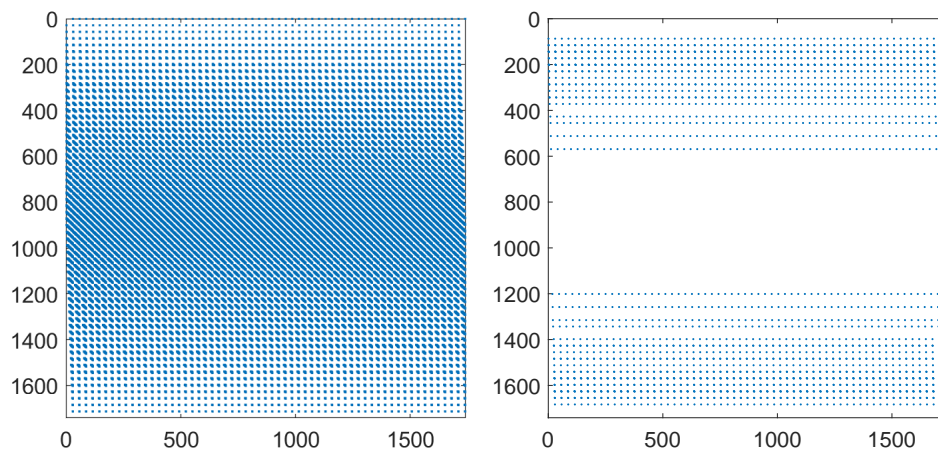

Figure 8. *Sparsity of the matrix Λ_n^k for $k = 2^4$ (left) and $k = 2^{11}$ (right). Rows represent different (θ_r, θ_o), and columns represent different (θ_s, θ_i). Elements that are larger than half of the maximal element in Λ_n^k are shown. For $k = 2^4$, we use a larger computational domain $[-8, 8]^2$, and the step size is $h = 2^{-8}$.*
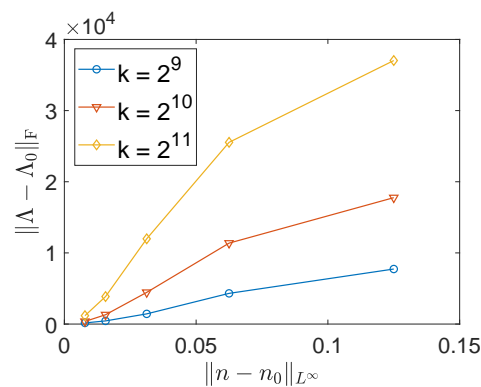

Figure 9. *The dependence of $\|\Lambda^k - \Lambda_0^k\|_F$ on the medium perturbation $\|n - n_0\|_{L^\infty}$. Different $\|n - n_0\|_{L^\infty}$ are obtained by tuning the amplitude A in the medium (4.8).*

$$(5.2) \qquad \min_n \mathcal{J}[n], \qquad \text{where} \qquad \mathcal{J}[n] := \frac{1}{2n_{\mathtt{rcv}}n_{\mathtt{src}}} \sum_{i=1}^{n_{\mathrm{rcv}}} \sum_{j=1}^{n_{\mathrm{src}}} \left| D^{i,j} - \left(\mathcal{D}^k[n] \right)^{i,j} \right|^2 .$$

In particular, $n_{\mathtt{rcv}}$ and $n_{\mathtt{src}}$ stand for the number of receivers and sources, and each point $(\mathcal{D}^k[n])^{i,j}$ is the intensity squared of the impulse response generated by illuminating the medium n with a tight beam given by (2.4) originated at x_{s}^i with direction v_{s}^i, which is then filtered using (2.6) centered at x_{r}^j with direction v_{r}^j. See the definition in (4.3) with $(x_{\mathrm{r}}, v_{\mathrm{r}})$ replaced by $(x_{\mathrm{r}}^j, v_{\mathrm{r}}^j)$, and u^k solving (4.1) with $(x_{\mathrm{s}}, v_{\mathrm{s}})$ replaced by $(x_{\mathrm{s}}^i, v_{\mathrm{s}}^i)$.

We employ quasi-Newton methods for finding a local minimum,[4] thus we need to efficiently compute the gradient of the misfit function. In order to provide a fully self-contained exposition we briefly summarize below how to compute the gradient for only one data point using the adjoint-state methods. From there the computation for the full gradient can be easily deduced.

We can readily compute the application of the gradient to a perturbation δn by using the chain rule, which results in

$$(5.3) \quad \nabla \mathcal{J}[n]\delta n = \left(\frac{k}{2\pi} \right)^d \left(D - H^k u^k(x_{\mathrm{r}}, v_{\mathrm{r}}) \right) \mathrm{Real} \left(2\overline{(u^k * \phi_{v_{\mathrm{r}}}^k(x_{\mathrm{r}}))}(\phi_{v_{\mathrm{r}}}^k(x_{\mathrm{r}}) * F[n]\delta n) \right),$$

where $F[n]$ is a linearized forward wave-propagation operator, given by the Born approximation of the scattered wavefield [10]. Thus the gradient can be easily computed by applying the adjoint of the Born approximation to the residual times the filter function, i.e.,

$$\nabla \mathcal{J}[n] = 2 \left(\frac{k}{2\pi} \right)^d \mathrm{Real} \left(F[n]^* \left((D - H^k u^k(x_{\mathrm{r}}, v_{\mathrm{r}}))(u^k * \phi_{v_{\mathrm{r}}}^k(x_{\mathrm{r}})\overline{(\phi_{v_{\mathrm{r}}}^k(x_{\mathrm{r}} - x))}) \right) \right).$$

Fortunately, the application of the adjoint of the Born approximation operator is well studied: it can be performed by solving the adjoint equation followed by a multiplication by the solution of the forward wave problem.[5] In this case the adjoint equation is the same Helmholtz equation, but with adjoint Sommerfeld radiation conditions, i.e., we solve

$$(5.4) \qquad \begin{aligned} \Delta v + k^2 n(x)v &= \left(D - H^k u^k(x_{\mathrm{r}}, v_{\mathrm{r}}) \right)(u^k * \phi_{v_{\mathrm{r}}}^k(x_{\mathrm{r}}))\overline{(\phi_{v_{\mathrm{r}}}^k(x_{\mathrm{r}} - x))}, \quad x \in \mathbb{R}^d, \\ \frac{\partial v}{\partial r} + \mathrm{i}kv &= \mathcal{O}(r^{-(d+1)/2}) \text{ as } r = |x| \to \infty. \end{aligned}$$

Thus, using (5.4), we can easily compute the application of the adjoint of the Born approximation

$$(5.5) \qquad F[n]^* \left((D - H^k u^k(x_{\mathrm{r}}, v_{\mathrm{r}}))(u^k * \phi_{v_{\mathrm{r}}}^k(x_{\mathrm{r}})\overline{(\phi_{v_{\mathrm{r}}}^k(x_{\mathrm{r}} - x))}) \right) = \overline{u^k}v,$$

where v solves (5.4).

We point out that in (5.5), the source for the adjoint is conjugated, thus following (2.6), we can see that it means that the $\overline{(\phi_{v_{\mathrm{r}}}^k(x - x_{\mathrm{r}}))}$ is pointing towards the interior of the domain in direction $-v_{\mathrm{r}}$.

---

[4]Given that the problem is very nonlinear, there is no guarantee that we can find the global minimum.
[5]We redirect the interested readers to [9] for a modern self-contained presentation.

We solve (5.2) using L-BFGS [11, 56], a quasi-Newton method in MATLAB. We consider the initial perturbation equal to zero. We set a first-order optimality tolerance of 10^{-5} and let the algorithm run for a maximum of 300 iterations or until the tolerance is achieved.

To avoid the inverse crime [20], the data are generated by solving the Lippmann–Schwinger equation discretized by the truncated kernel method [50] as in section 4, and the inversion is performed with a fourth-order finite difference scheme for both (4.1) and (5.4). To generate the data, we set the computational domain to be $K = [-1,1]^2$ with $N_{\mathrm{LS}} = 256^2 = 65536$ grid points so that there are at least 12 points per wavelength for the largest $k = 2^6$. In the inversion, we discretize the same domain K with $N_{\mathrm{FD}} = 163^2 = 26569$ grid points so that there are at least 8 points per wavelength for $k = 2^6$. We enclose the domain K with a perfect matching layer (PML) to avoid reflection. We choose the thickness of PML to be 2.5 times wavelength.

The measurement is taken on $\partial B(R)$ with $R = 0.4$ in all the examples. To generate the probing ray, we set $\sigma = 2^{-2}$ in (4.2). We compute the data with the source position and incident direction

$$x_{\mathrm{s}}^{i_1} = (R \cos \theta_{\mathrm{s}}^{i_1}, R \sin \theta_{\mathrm{s}}^{i_1}),$$
$$v_{\mathrm{s}}^{i_1,i_2} = (-\cos(\theta_{\mathrm{s}}^{i_1} + \theta_{\mathrm{i}}^{i_2}), -\sin(\theta_{\mathrm{s}}^{i_1} + \theta_{\mathrm{i}}^{i_2})),$$

where $\theta_{\mathrm{s}}^{i_1} = \pi + i_1 \frac{\pi}{48}$ for all $i_1 = 0, \ldots, 95$ and $\theta_{\mathrm{i}}^{i_2} = -\frac{\pi}{2} + i_2 \frac{\pi}{49}$ for all $i_2 = 1, \ldots, 48$, and the receiver position

$$x_{\mathrm{r}}^{j_1} = (R \cos \theta_{\mathrm{r}}^{j_1}, R \sin \theta_{\mathrm{r}}^{j_1}),$$
$$v_{\mathrm{r}}^{j_1,j_2} = (\cos(\theta_{\mathrm{r}}^{j_1} + \theta_{\mathrm{o}}^{j_2}), \sin(\theta_{\mathrm{r}}^{j_1} + \theta_{\mathrm{o}}^{j_2})),$$

where $\theta_{\mathrm{r}}^{j_1} = j_1 \frac{\pi}{48}$ for all $j_1 = 0, \ldots, 95$ and $\theta_{\mathrm{o}}^{j_2} = -\frac{\pi}{2} + j_2 \frac{\pi}{49}$ for all $j_2 = 1, \ldots, 48$.

In all the examples, the scattered data are perturbed with the noise in the form

$$(5.6) \qquad \widetilde{D}^{i,j} = D^{i,j} + 0.05\varepsilon \frac{D^{i,j}}{|D^{i,j}|},$$

where ε is a symmetric Bernoulli random variable that takes the values ± 1.

All the experiments are reported on a server with 64-core Intel Xeon CPU and 256 Gigabytes RAM. The codes accompanying this manuscript are publicly available [13].

In order to illustrate the reconstruction using Husimi data, we choose three examples of increasing complexity. The exact contrast function $q(x)$'s are shown in Figure 10.

In the first example, we consider a single bump in the form (4.8) with $A = 0.5$ and $r = 0.2$, which is shown in Figure 10 (left). We run the minimization loop as described above using $k = 2^4$ and $k = 2^6$, and the resulting reconstructions are shown in Figure 11. From Figure 11 we can clearly see that as k becomes larger, the reconstruction becomes closer to the true medium. The solution time for $k = 2^6$ is 15787.1 seconds.

In the second example, we consider a delocalized medium. The delocalized contrast function $q(x)$ is obtained by convolving a pointwise independent Gaussian random field with a Gaussian mollifier. The main difference with the single bump example is that the refractive index, can be smaller than the background one, thus allowing for more complex ray paths as
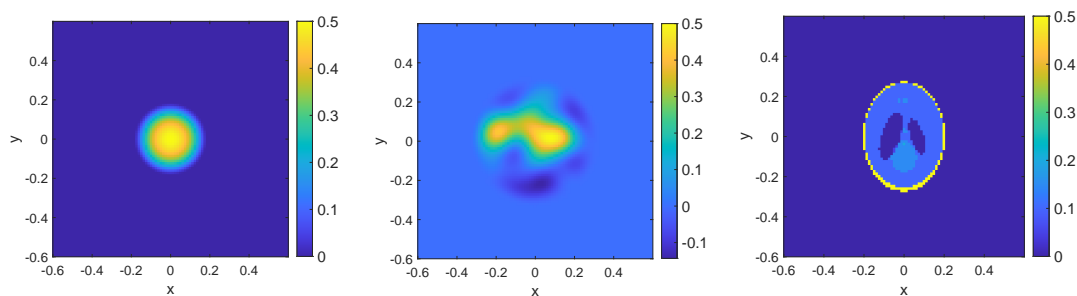
Figure 10. *The contrast function $q(x)$ for our three examples: a bump function (left), a delocalized function (middle), and the Shepp–Logan phantom (right).*
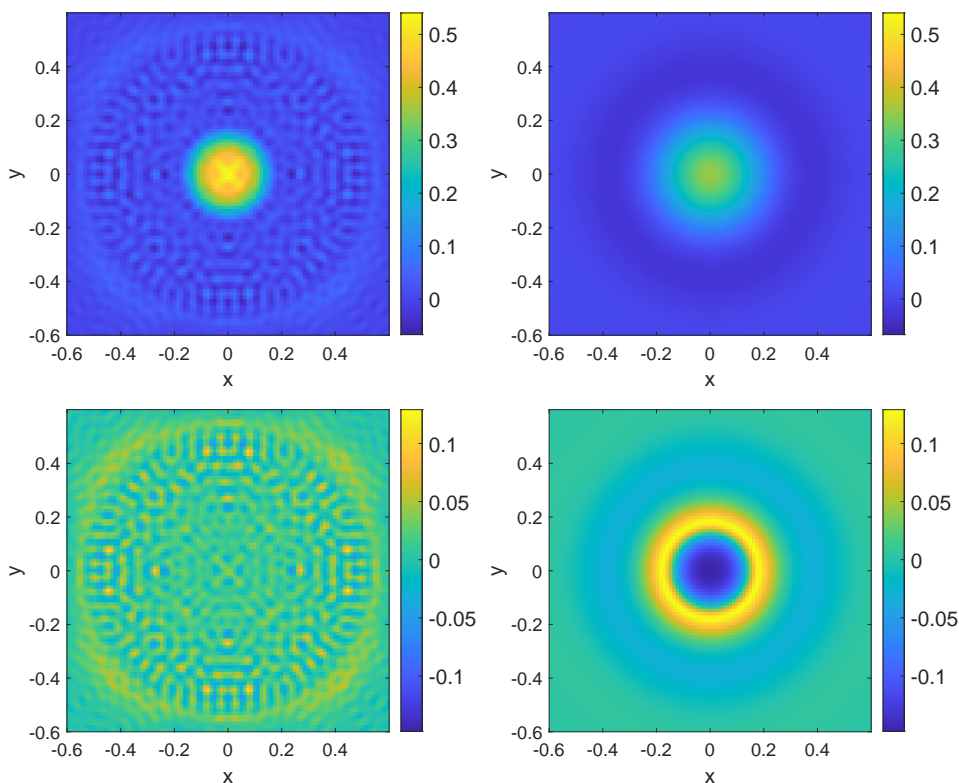

Figure 11. *Recovering a single bump contrast function. The upper row shows the estimated contrast function and the lower row shows the reconstruction error at $k = 2^6$ (left) and $k = 2^4$ (right).*

shown in Figure 10 (center). We repeat the same experiments, whose results are shown in Figure 12. The solution time required for $k = 2^6$ is 13185.3 seconds.

Finally, for the third example, we consider the more challenging, and more practical, problem of recovering the Shepp–Logan phantom, depicted in Figure 10 (right). In this case we have very sharp transitions of the refractive index, which will generate a strong reflection, compared to the refraction-dominated media considered before. In addition, the interior of the still acts as a resonant cavity, thus creating a large number of interior reflections, which
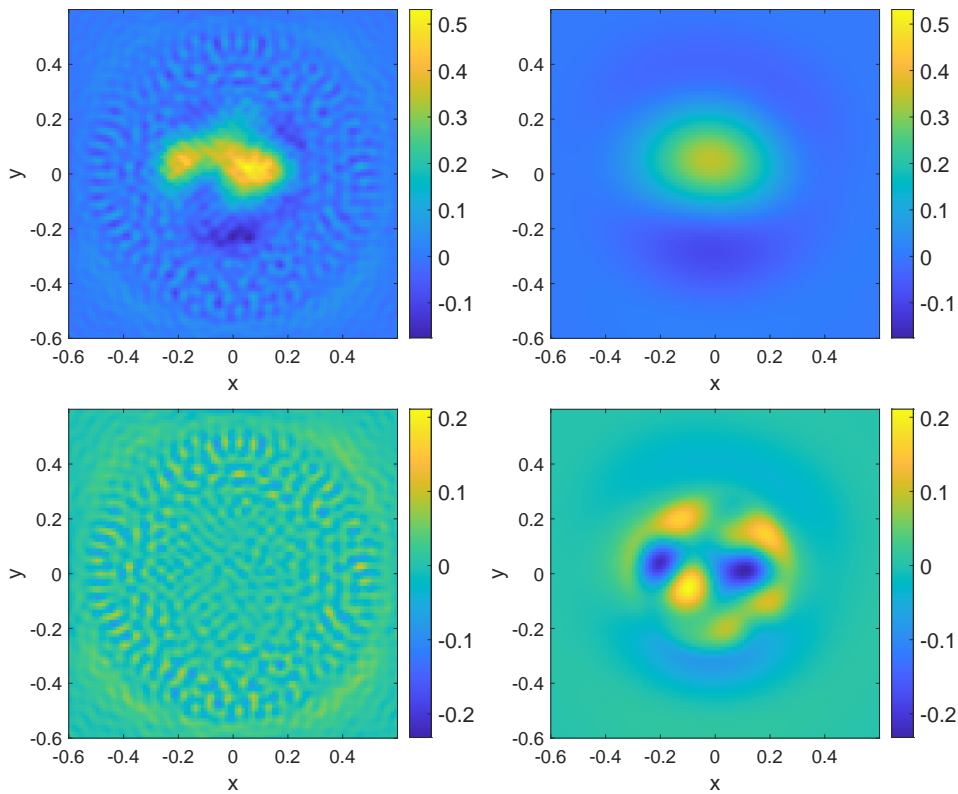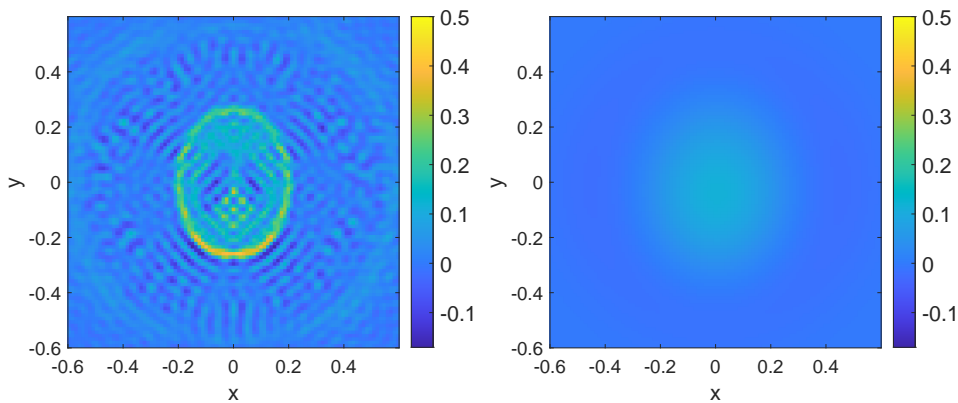
Figure 12. *Recovering a delocalized contrast function. The upper row shows the estimated contrast function and the lower row shows the reconstruction error at $k = 2^6$ (left) and $k = 2^4$ (right).*

Figure 13. *Recovering the Shepp–Logan phantom. The estimated contrast functions are shown for $k = 2^6$ (left) and $k = 2^4$ (right).*

are exacerbated as the frequency increases. We perform the same experiments as above, whose results are depicted in in Figure 13. The solution time required for $k = 2^6$ is 14640.4 seconds. In this case, the reconstruction is qualitatively worse than before. We can still see the shape of the phantom, but with a large amount of artifacts. These artifacts are common to the
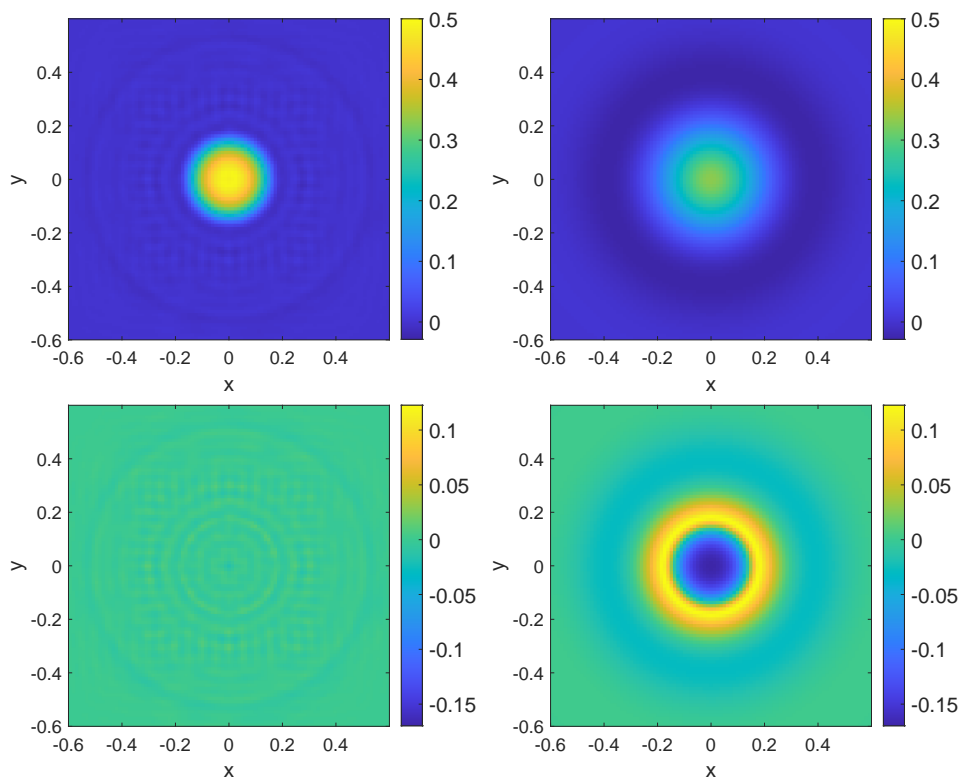
Figure 14. *Recovering a single bump contrast function with a 4th-order finite difference solver for both data and inversion. The upper row shows the estimated contrast function and the lower row shows the reconstruction error at $k = 2^6$ (left) and $k = 2^4$ (right).*

three examples, but are somewhat more notorious for the Shepp–Logan phantom. Indeed, these artifacts can in part be explained by the large difference in the dispersion relation between the forward and backwards discretization. The Lippmann–Schwinger discretization used for the forward problem is known to be highly accurate if the media is smooth. In the previous cases, the data generated by the Lippmann–Schwinger solver is close to the analytical solution, and the artifacts seems to come mostly for the phase errors in the finite-difference discretization. However, in this case the phantom is discontinuous thus creating large phase errors in the solution of the equation, and therefore the forward map, which in return produce more notorious artifacts.

To avoid inverse crime, we have used two different solvers for computing the equation. The two solvers produce relatively large phase errors that propagate in the reconstruction. The reconstruction can be significantly improved if we use the same PDE solvers in generating data and reconstructing the media. In Figure 14, we show the reconstructions of the same single bump medium as in Figure 11 but with the fourth-order finite difference for both data generation and inversion. It can be seen that the artifacts in the estimated medium are much smaller for larger k and the reconstructed medium achieves a relative L^2 error of 0.0389 for $k = 2^6$. Better reconstruction can also be seen in Figure 15 for the reconstructed delocalized medium, whose relative L^2 error is 0.0341 for $k = 2^6$. In Figure 16, we show the
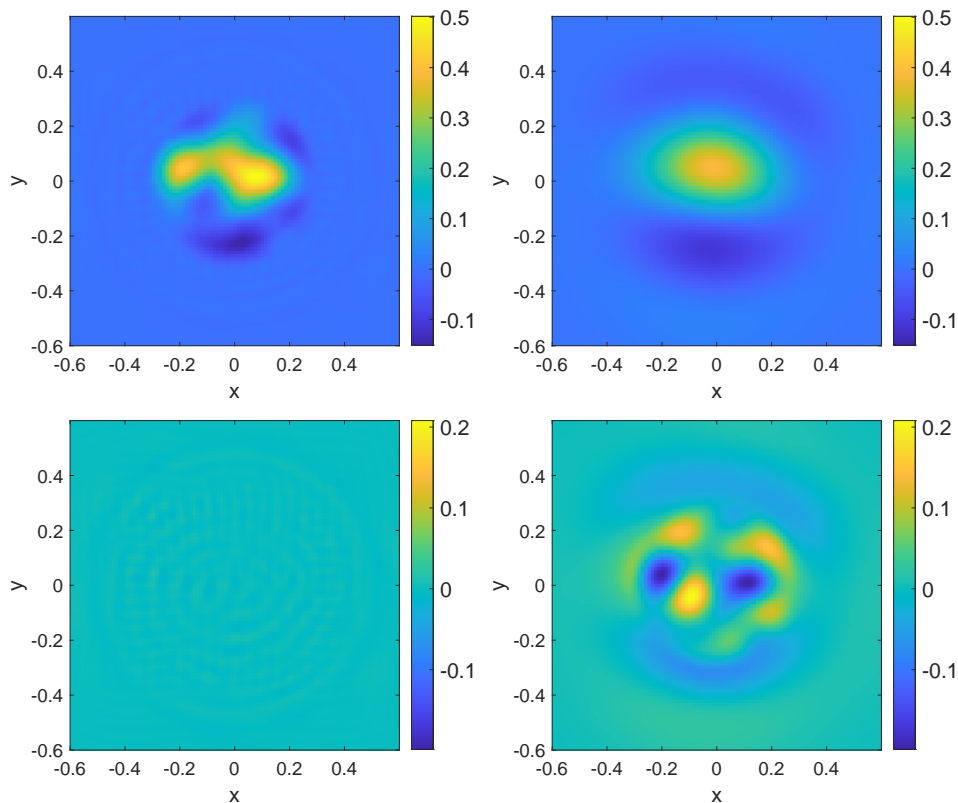
Figure 15. *Recovering a delocalized contrast function with a 4th-order finite difference solver for both data and inversion. The upper row shows the estimated contrast function and the lower row shows the reconstruction error at $k = 2^6$ (left) and $k = 2^4$ (right).*

reconstruction for the Shepp–Logan phantom. We can observe that as the frequency increases the reconstruction becomes better, though due to computational limitations induced by the current implementation, we were unable to test with a higher frequency. However, we would expect to obtain even a better reconstruction.

Last, we compare the conventional inverse scattering problem and our new inverse problem using the Husimi data. We choose the incident wave $u^{i,k} = e^{i\omega\hat{\theta}\cdot x}$ with $\hat{\theta} \in \mathbb{S}^1$ in (2.2), and measure the scattered far field data $u^{s,k}$. Again we cast the problem as a nonlinear least squares problem, and solve it using L-BFGS. We consider the initial perturbation equal to zero, and set a first-order optimality tolerance of 10^{-5}.

For simplicity, we use a fourth-order finite difference for both data generation and inversion. The setup of the computational domain and the discretization are the same as in the previous examples.

The far-field measurement is taken on the boundary $\partial B(\widetilde{R})$ with $\widetilde{R} = 1$. We compute the data with 180 incident directions $\hat{\theta}$ that are equally distributed on $\mathbb{S}^1$ and 180 receivers that are equally distributed on $\partial B(\widetilde{R})$. We add 5% noise to the scattered data in the form of (5.6).

Finally, we test the robustness of the new formulation with respect to the nonconvexity of the loss function. The ill-posedness of the inverse scattering problem is often manifested as a very nonconvex loss function with a myriad of local minima. As a consequence, any
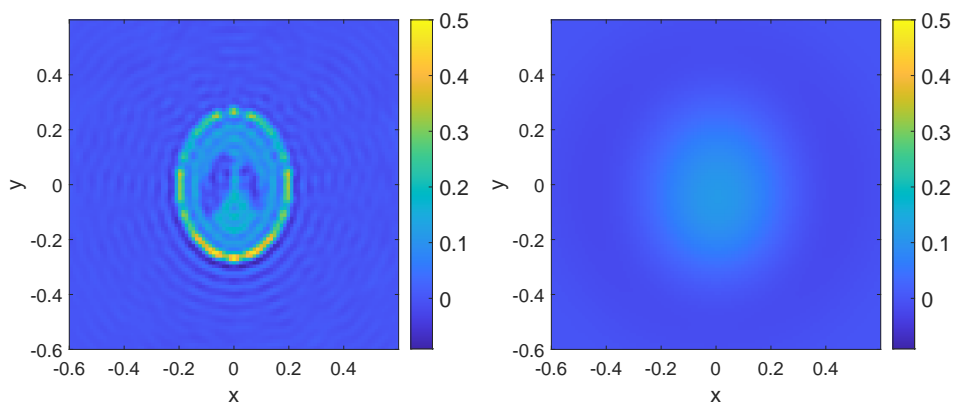
Figure 16. *Recovering the Shepp–Logan phantom with a 4th-order finite difference solver for both data and inversion. The estimated contrast functions are shown for $k = 2^6$ (left) and $k = 2^4$ (right).*
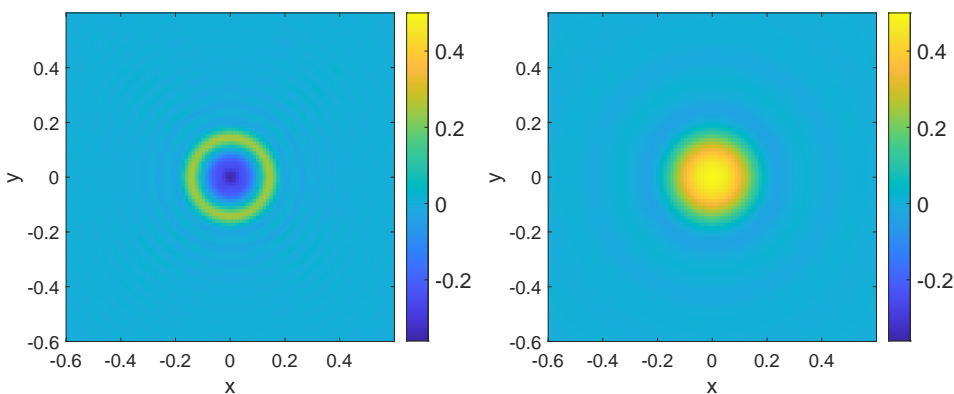

Figure 17. *Recovering a single bump contrast function by plane waves. The estimated contrast function at $k = 2^6$ (left) and $k = 2^4$ (right) are shown. A 4th-order finite difference solver is used for both data and inversion.*
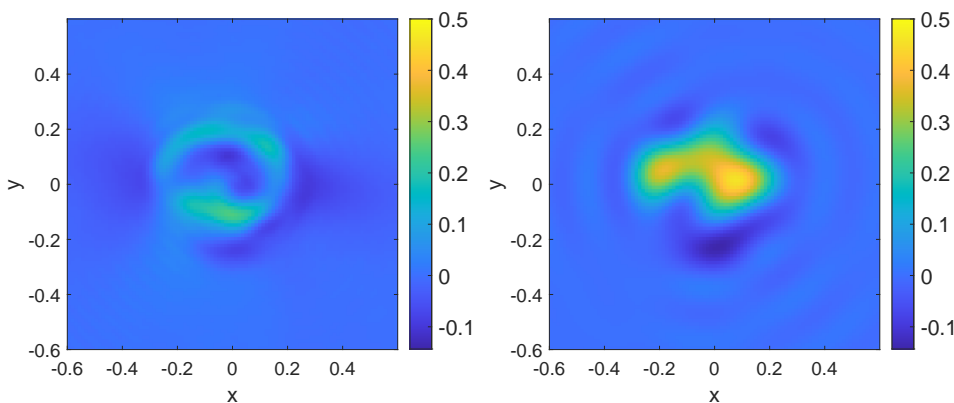

Figure 18. *Recovering a delocalized contrast function by plane wave. The estimated contrast function at $k = 2^6$ (left) and $k = 2^4$ (right) are shown. A 4th-order finite difference solver is used for both data and inversion.*

Figure 19. *Recovering the Shepp–Logan phantom by plane wave. The estimated contrast function at $k = 2^6$ (left) and $k = 2^4$ (right) are shown.* A 4*th-order finite difference solver is used for both data and inversion.*
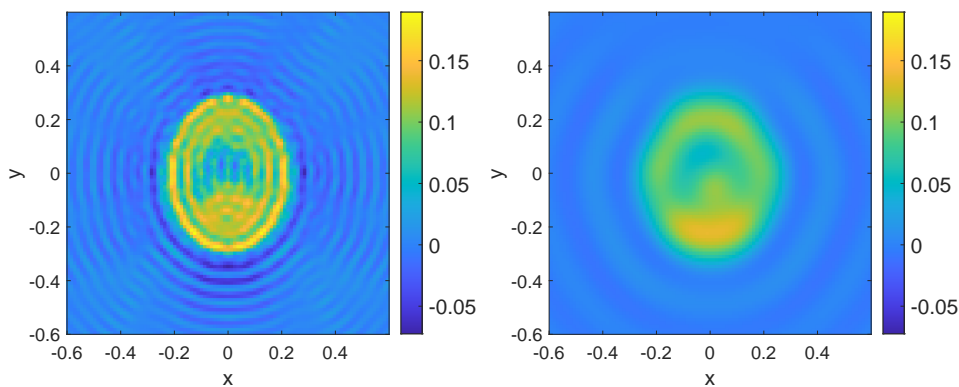
PDE constrained optimization-based reconstruction has a higher chance of converging to a nonphysical minimum, a process that is often called cycle skipping [51]. For comparing the new formulation and the traditional one we also run the classical full-wave form inversion in the frequency domain, using data at a single frequency, using the delocalized media in Figure 10. As discussed in section 2.1.1, in the classical formulation one probes the medium with plane waves, and the measurement operator samples the wavefield directly on the boundary of the domain of interest. Numerically, we minimize the ℓ^2 misfit of the wavefield at the boundary, using the same L-BFGS solver as before. The initial guess is zero. We repeat the experiments for two different wave numbers that are used in the new formulation as well. The results are shown in Figures 17, 18, and 19, respectively. In the plots we can observe that at low frequencies we recover a smoothed version of the medium, but as the frequency increases we encounter cycle skipping, i.e., the algorithm converges to a spurious medium. This is a stark contrast to the inversion results of the new formulation shown in Figures 14, 15, and 16, where at low frequency the reconstruction does not perform as well, but it is more stable at high frequencies, providing an accurate reconstruction.

In summary the numerical experiments seem to indicate that the new inverse formulation is far more robust to cycle skipping than its traditional counterpart.

6. Conclusions. To reconstruct an unknown medium, the generalized Helmholtz inverse scattering problem uses data pairs consisting of the impinging and scattered wave fields, while the Liouville inverse scattering problems use data pairs consisting of incoming and outgoing wave location and direction. The former is regarded as ill-posed in the high-frequency regime, while the latter is well-posed. This is intuitively contradicting the fact that the Liouville equation is the asymptotic limit of the Helmholtz equation.

We investigate this issue in this paper. In particular, we develop a new formulation for studying the Helmholtz inverse scattering problem with a new data collection process, and we show that this new formulation, in the high-frequency limit, becomes the Liouville inverse scattering problem, and thus inherits the well-posedness nature. This discovery bares the conceptual merit of providing the mathematical description of the wave-particle duality for light propagation in the inverse setting. In addition, this discovery also suggests a more stable

numerical reconstruction process for studying the Helmholtz inverse scattering problem, which we showcase using several numerical experiments.

Appendix A. Formal derivation of Theorem 3.1. We start from the equation

$$(A.1) \qquad ik\alpha^k u^k + \Delta u^k + k^2 n(x)u^k = -S^k(x) = -k^{\frac{d+3}{2}} S(k(x - x_s)), \quad x \in \mathbb{R}^d,$$

and assume that $\alpha^k \to \alpha \geq 0$ in the limit $k \to \infty$. We denote the density matrix of u^k satisfying (A.1) by

$$(A.2) \qquad g^k(x, y) = u^k\left(x - \frac{y}{2k}\right) \overline{u^k}\left(x + \frac{y}{2k}\right),$$

and the Fourier transform of a generic u by

$$(A.3) \qquad \widehat{u}(v) = \mathcal{F}_{y \to v} u(y) = \frac{1}{(2\pi)^d} \int_{\mathbb{R}^d} e^{-iyv} u(y)\mathrm{d}y.$$

The inverse Fourier transform is then

$$(A.4) \qquad \mathcal{F}_{v \to x}^{-1} u(v) = \int_{\mathbb{R}^d} e^{ixv} u(v)\mathrm{d}v.$$

Now we compute the equation satisfied by the Wigner transform. The first step is to compute the derivatives of g^k,

$$(A.5) \quad \nabla_y \cdot \nabla_x g^k(x, y) = -\frac{1}{2k}\left[\Delta u^k\left(x - \frac{y}{2k}\right) \overline{u^k}\left(x + \frac{y}{2k}\right) - u^k\left(x - \frac{y}{2k}\right) \Delta\overline{u^k}\left(x + \frac{y}{2k}\right)\right],$$

and thus we have

$$
\begin{aligned}
\alpha^k g^k + i\nabla_y \cdot \nabla_x g^k(x, y) &+ \frac{ik}{2}\left[n\left(x + \frac{y}{2k}\right) - n\left(x - \frac{y}{2k}\right)\right] g^k(x, y) \\
(A.6) \qquad &= \sigma^k(x, y) \\
&:= \frac{i}{2k}\left[S^k\left(x - \frac{y}{2k}\right) \overline{u^k}\left(x + \frac{y}{2k}\right) - \overline{S^k}\left(x + \frac{y}{2k}\right) u^k\left(x - \frac{y}{2k}\right)\right].
\end{aligned}
$$

Therefore, after a Fourier transform, we obtain the following transport equation on the Wigner transform f^k,

$$(A.7) \qquad \alpha^k f^k(x, v) + v \cdot \nabla_x f^k(x, v) + Z^k(x, v) *_v f^k(x, v) = Q^k(x, v),$$

where the last term denotes the convolution in v,

$$Z^k(x, v) *_v f^k(x, v) = \int_{\mathbb{R}^d} Z^k(x, v - p) f^k(x, p)\mathrm{d}p,$$

and the quantities Z^k, Q^k arising in this equation are given by

$$
\begin{aligned}
(A.8) \qquad Z^k(x, v) &= \frac{1}{(2\pi)^d} \frac{ik}{2} \mathcal{F}_{y \to v}^{-1}\left[n\left(x + \frac{y}{2k}\right) - n\left(x - \frac{y}{2k}\right)\right], \\
Q^k(x, v) &= \frac{1}{(2\pi)^d} \mathcal{F}_{y \to v}^{-1} \sigma^k(x, y).
\end{aligned}
$$

From this equation we can formally compute the limits. For Z^k we have that

$$(A.9) \qquad Z^k(x,v) \xrightarrow{k\to\infty} \frac{1}{(2\pi)^d} \frac{i}{2} (\mathcal{F}_{y\to v}^{-1} y) \cdot \nabla_x n(x) = -\frac{1}{2} \nabla_x n(x) \cdot \nabla_v \delta(v).$$

The limit of the source term Q^k is slightly more involved. First, we define the complex-valued function

$$(A.10) \qquad w^k(y) = \frac{1}{k^{\frac{d-1}{2}}} u^k \left(x_s + \frac{y}{k} \right),$$

which after a change of variable can be rewritten as

$$(A.11) \qquad u^k(x) = k^{\frac{d-1}{2}} w^k(k(x - x_s)),$$

where function w^k satisfies the rescaled Helmholtz equation

$$(A.12) \qquad i\frac{\alpha^k}{k} w^k + \Delta w^k + n\left(x_s + \frac{y}{k} \right) w^k = -S(y).$$

In the high-frequency limit, w^k converges towards a solution w of

$$(A.13) \qquad \Delta w + n(x_s)w = -S(y).$$

The second step is to compute the Fourier transform of w. To do so, we add an absorption term to the equation above, resulting in

$$(A.14) \qquad i\beta w + \Delta w + n(x_s)w = -S(y),$$

where $\beta > 0$. This new term is used as a broadening factor, which helps to smooth the Fourier transform. We perform a Fourier transform on both sides, which leads to

$$(A.15) \qquad \widehat{w}(v) = \frac{-\hat{S}(v)}{n(x_s) - |v|^2 + i\beta} = \hat{S}(v)\hat{G}(v;\beta),$$

where $\hat{G}(v;\beta)$ denotes the Fourier transform of the outgoing Green's function that vanishes at infinity:

$$(A.16)$$
$$\hat{G}(v;\beta) \equiv -\frac{1}{n(x_s) - |v|^2 + i\beta} = -\frac{n(x_s) - |v|^2}{(n(x_s) - |v|^2)^2 + \beta^2} + \frac{i\beta}{(n(x_s) - |v|^2)^2 + \beta^2}, \quad \beta > 0.$$

As usual, we take the limit $\beta \to 0+$. The first term converges weakly to the principal value (P.V.)

$$(A.17) \qquad -\frac{n(x_s) - |v|^2}{(n(x_s) - |v|^2)^2 + \beta^2} \xrightarrow{\beta\to 0+} -\text{P.V.}\left(\frac{1}{n(x_s) - |v|^2} \right).$$

The second term converges to a delta function on the sphere $\{|v|^2 = n(x_s)\}$ as $\beta \to 0+$:

$$(A.18) \qquad \frac{i\beta}{(n(x_s) - |v|^2)^2 + \beta^2} \xrightarrow{\beta\to 0+} \frac{i\pi}{2} \delta(|v|^2 = n(x_s)).$$

In summary, we obtain the Fourier transform of the outgoing solution to (A.13):

$$(A.19) \quad \widehat{w}(v) = \lim_{\beta \to 0+} \hat{S}(v)\hat{G}(v;\beta) = \hat{S}(v)\left[\frac{i\pi}{2}\delta(|v|^2 = n(x_s)) - \text{P.V.}\left(\frac{1}{n(x_s) - |v|^2}\right)\right].$$

Now we are ready to compute Q^k. We take two test functions $\phi(x)$ and $\psi(y)$:

$$\int_{\mathbb{R}^{2d}} \sigma^k(x,y)\phi(x)\psi(y)\,\mathrm{d}x\,\mathrm{d}y$$

$$= \frac{i}{2k}\int_{\mathbb{R}^{2d}}\left[S^k\left(x - \frac{y}{2k}\right)\overline{u^k}\left(x + \frac{y}{2k}\right) - \overline{S^k}\left(x + \frac{y}{2k}\right)u^k\left(x - \frac{y}{2k}\right)\right]\phi(x)\psi(y)\mathrm{d}x\mathrm{d}y$$

$$\begin{aligned}(A.20) \quad &= \frac{ik^d}{2}\int_{\mathbb{R}^d}\left[S\left(k\left(x - \frac{y}{2k} - x_s\right)\right)\overline{w^k}\left(k\left(x + \frac{y}{2k} - x_s\right)\right)\right. \\ &\qquad\qquad \left. - \overline{S}\left(k\left(x + \frac{y}{2k} - x_s\right)\right)w^k\left(k\left(x - \frac{y}{2k} - x_s\right)\right)\right]\phi(x)\psi(y)\mathrm{d}x\mathrm{d}y\end{aligned}$$

$$= \frac{i}{2}\int_{\mathbb{R}^{2d}}\left[S(z)\overline{w^k}(z+y)\phi\left(\frac{z}{k} + \frac{y}{2k} + x_s\right) - \overline{S}(z)w^k(z-y)\phi\left(\frac{z}{k} - \frac{y}{2k} + x_s\right)\right]\psi(y)\mathrm{d}z\mathrm{d}y$$

$$\xrightarrow{k\to\infty} \frac{i}{2}\phi(x_s)\int_{\mathbb{R}^{2d}}\left[S(z)\overline{w}(z+y) - \overline{S}(z)w(z-y)\right]\psi(y)\mathrm{d}z\mathrm{d}y.$$

In other words, we have formally obtained that

$$(A.21) \qquad \sigma^k(x,y) \xrightarrow{k\to\infty} \frac{i}{2}\delta(x - x_s)\int_{\mathbb{R}^d}\left[S(z)\overline{w}(z+y) - \overline{S}(z)w(z-y)\right]\mathrm{d}z,$$

which after a Fourier transform gives

$$Q^k(x,v) = \frac{1}{(2\pi)^d}\mathcal{F}^{-1}_{y\to v}\sigma^k(x,y)$$

$$\begin{aligned}(A.22) \quad &\xrightarrow{k\to\infty} \frac{1}{(2\pi)^d}\frac{i}{2}\delta(x - x_s)\mathcal{F}^{-1}_{y\to v}\left\{\int_{\mathbb{R}^d}\left[S(z)\overline{w}(z+y) - \overline{S}(z)w(z-y)\right]\mathrm{d}z\right\} \\ &= \frac{i}{2}\delta(x - x_s)(2\pi)^d\left[\hat{S}(v)\overline{\widehat{w}(v)} - \overline{\hat{S}(v)}\widehat{w}(v)\right] \\ &= (2\pi)^d\delta(x - x_s)\text{Im}\left[\overline{\hat{S}(v)}\widehat{w}(v)\right].\end{aligned}$$

We finally obtain

$$(A.23) \qquad Q^k(x,v) \xrightarrow{k\to\infty} (2\pi)^d\frac{\pi}{2}\delta(x - x_s)|\hat{S}(v)|^2\delta(|v|^2 = n(x_s))$$

by substituting (A.19) in (A.22).

REFERENCES

[1] R. Alaifari, I. Daubechies, P. Grohs, and R. Yin, *Stable phase retrieval in infinite dimensions*, Found. Comput. Math., 19 (2019), pp. 869–900.

[2] D. Atkinson and N. D. Aparicio, *An inverse problem method for crack detection in viscoelastic materials under anti-plane strain*, Internat. J. Engrg. Sci., 35 (1997), pp. 841–849.

[3] G. BAL, G. PAPANICOLAOU, AND L. RYZHIK, *Radiative transport limit for the random Schrödinger equation*, Nonlinearity, 15 (2002), pp. 513–529.

[4] G. BAL AND G. UHLMANN, *Inverse diffusion theory of photoacoustics*, Inverse Problems, 26 (2010), 085010.

[5] G. BAO, P. LI, J. LIN, AND F. TRIKI, *Inverse scattering problems with multi-frequencies*, Inverse Problems, 31 (2015), 093001.

[6] G. BAO AND H. ZHANG, *Sensitivity analysis of an inverse problem for the wave equation with caustics*, J. Amer. Math. Soc., 27 (2014), pp. 953–981.

[7] C. BARDOS, G. LEBEAU, AND J. RAUCH, *Sharp sufficient conditions for the observation, control, and stabilization of waves from the boundary*, SIAM J. Control Optim., 30 (1992), pp. 1024–1065.

[8] J.-D. BENAMOU, F. CASTELLA, T. KATSAOUNIS, AND B. PERTHAME, *High frequency limit of the Helmholtz equations*, Rev. Mat. Iberoam., 18 (2002), pp. 187–209.

[9] C. BORGES, A. GILLMAN, AND L. GREENGARD, *High resolution inverse scattering in two dimensions using recursive linearization*, SIAM J. Imaging Sci., 10 (2017), pp. 641–664.

[10] M. BORN, *Quantenmechanik der stoßvorgänge*, Z. Phys., 38 (1926), pp. 803–827.

[11] R. H. BYRD, P. LU, J. NOCEDAL, AND C. ZHU, *A limited memory algorithm for bound constrained optimization*, SIAM J. Sci. Comput., 16 (1995), pp. 1190–1208.

[12] F. CASTELLA, B. PERTHAME, AND O. RUNBORG, *High frequency limit of the Helmholtz equation. II. Source on a general smooth manifold*, Comm. Partial Differential Equations, 27 (2002), pp. 607–651.

[13] S. CHEN, Z. DING, Q. LI, AND L. ZEPEDA-NÚNEZ, *Inverse Scattering with Husimi Data*, https://github.com/Forgotten/inverse_scattering/tree/husimi, 2021.

[14] S. CHEN AND Q. LI, *Semiclassical limit of an inverse problem for the Schrödinger equation*, Res. Math. Sci., 8 (2021), pp. 1–18.

[15] S. CHEN, Q. LI, AND X. YANG, *Classical limit for the varying-mass Schrödinger equation with random inhomogeneities*, J. Comput. Phys., 438 (2021), 110365.

[16] Y. CHEN, *Inverse scattering via Heisenberg's uncertainty principle*, Inverse Problems, 13 (1997), pp. 253–282.

[17] M. CHENEY, *A mathematical tutorial on synthetic aperture radar*, SIAM Rev., 43 (2001), pp. 301–312.

[18] E. CHUNG, J. QIAN, G. UHLMANN, AND H. ZHAO, *A new phase space method for recovering index of refraction from travel times*, Inverse Problems, 23 (2007), pp. 309–329.

[19] A. COLLI, D. PRATI, M. FRAQUELLI, S. SEGATO, P. P. VESCOVI, F. COLOMBO, C. BALDUINI, S. DELLA VALLE, AND G. CASAZZA, *The use of a pocket-sized ultrasound device improves physical examination: Results of an in- and outpatient cohort study*, PLOS One, 10 (2015), pp. 1–10.

[20] D. L. COLTON AND R. KRESS, *Inverse Acoustic and Electromagnetic Scattering Theory*, Appl. Math. Sci. 93, Springer, Cham, Switzerland, 2019.

[21] M. COMBESCURE AND D. ROBERT, *Coherent States and Applications in Mathematical Physics*, Springer, Cham, Switzerland, 2012.

[22] M. DE BUHAN AND M. DARBAS, *Numerical resolution of an electromagnetic inverse medium problem at fixed frequency*, Comput. Math. Appl., 74 (2017), pp. 3111–3128.

[23] M. DE BUHAN AND M. KRAY, *A new approach to solve the inverse scattering problem for waves: Combining the TRAC and the adaptive inversion methods*, Inverse Problems, 29 (2013), 085009.

[24] B. ENGQUIST AND O. RUNBORG, *Computational high frequency wave propagation*, Acta Numer., 12 (2003), pp. 181–266.

[25] P. GÉRARD, P. A. MARKOWICH, N. J. MAUSER, AND F. POUPAUD, *Homogenization limits and Wigner transforms*, Comm. Pure Appl. Math., 50 (1997), pp. 323–379.

[26] P. GROHS, S. KOPPENSTEINER, AND M. RATHMAIR, *Phase retrieval: Uniqueness and stability*, SIAM Rev., 62 (2020), pp. 301–350.

[27] P. GROHS AND M. RATHMAIR, *Stable Gabor phase retrieval and spectral clustering*, Comm. Pure Appl. Math., 72 (2019), pp. 981–1043.

[28] P. HÄHNER AND T. HOHAGE, *New stability estimates for the inverse acoustic inhomogeneous medium problem and applications*, SIAM J. Math. Anal., 33 (2001), pp. 670–685.

[29] V. ISAKOV, *Inverse Problems for Partial Differential Equations*, Appl. Math. Sci. 127, 3rd ed., Springer, Cham, Switzerland, 2017.

[30] M. C. KING, *Principles of optical lithography*, VLSI Electron. Microstructure Sci., 1, (1981), pp. 41–81.

[31] A. KIRSCH, *An Introduction to the Mathematical Theory of Inverse Problems*, Appl. Math. Sci. 120, Springer, Cham, Switzerland, 2011.

[32] R.-Y. LAI, Q. LI, AND G. UHLMANN, *Inverse problems for the stationary transport equation in the diffusion scaling*, SIAM J. Appl. Math., 79 (2019), pp. 2340–2358.

[33] Y. E. LI AND L. DEMANET, *Full-waveform inversion with extrapolated low-frequency data*, Geophysics, 81 (2016), pp. R339–R348.

[34] J. LU AND X. YANG, *Frozen Gaussian approximation for high frequency wave propagation*, Commun. Math. Sci., 9 (2010), pp. 663–683.

[35] F. MONARD, P. STEFANOV, AND G. UHLMANN, *The geodesic ray transform on Riemannian surfaces with conjugate points*, Commun. Math. Phys., 337 (2015), pp. 1491–1513.

[36] S. NAGAYASU, G. UHLMANN, AND J.-N. WANG, *Increasing stability in an inverse problem for the acoustic equation*, Inverse Problems, 29 (2013), 025012.

[37] F. NATTERER, *The Mathematics of Computerized Tomography*, Classics Appl. Math. 32, SIAM, Philadelphia, 2001.

[38] R. G. NOVIKOV, *Small angle scattering and X-ray transform in classical mechanics*, Ark. Mat., 37 (1999), pp. 141–169.

[39] R. D. OLDHAM, *The constitution of the interior of the earth, as revealed by earthquakes*, Quart. J. Geol. Soc., 62 (1906), pp. 456–475.

[40] J. R. PETTIT, A. E. WALKER, AND M. J. S. LOWE, *Improved detection of rough defects for ultrasonic nondestructive evaluation inspections based on finite element modeling of elastic wave scattering*, IEEE Trans. Ultrason. Ferroelectric Freq. Control, 62 (2015), pp. 1797–1808.

[41] R. G. PRATT, *Seismic waveform inversion in the frequency domain; Part 1: Theory and verification in a physical scale model*, Geophysics, 64 (1999), pp. 888–901.

[42] J. QIAN AND L. YING, *Fast multiscale Gaussian wavepacket transforms and multiscale Gaussian beams for the wave equation*, Multiscale Model. Simul., 8 (2010), pp. 1803–1837.

[43] N. RAWLINSON, S. POZGAY, AND S. FISHWICK, *Seismic tomography: A window into deep earth*, Phys. Earth Planet. Interiors, 178 (2010), pp. 101–135.

[44] L. RYZHIK, G. PAPANICOLAOU, AND J. B. KELLER, *Transport equations for elastic and other waves in random media*, Wave Motion, 24 (1996), pp. 327–370.

[45] H. SCHOMBERG, *An improved approach to reconstructive ultrasound tomography*, J. Phys. D, 11 (1978), pp. L181–L185.

[46] P. STEFANOV, G. UHLMANN, A. VASY, AND H. ZHOU, *Travel time tomography*, Acta Math. Sinica (English Ser.), 35 (2019), pp. 1085–1114.

[47] Z. SUN, *On continuous dependence for an inverse initial boundary value problem for the wave equation*, J. Math. Anal. Appl., 150 (1990), pp. 188–204.

[48] N. M. TANUSHEV, J. QIAN, AND J. V. RALSTON, *Mountain waves and Gaussian beams*, Multiscale Model. Simul., 6 (2007), pp. 688–709.

[49] A. TARANTOLA, *Inversion of seismic reflection data in the acoustic approximation*, Geophysics, 49 (1984), pp. 1259–1266.

[50] F. VICO, L. GREENGARD, AND M. FERRANDO, *Fast convolution with free-space Green's functions*, J. Comput. Phys., 323 (2016), pp. 191–203.

[51] J. VIRIEUX, A. ASNAASHARI, R. BROSSIER, L. MÉTIVIER, A. RIBODETTI, AND W. ZHOU, *6. An introduction to full waveform inversion*, in Encyclopedia of Exploration Geophysics, Society of Exploration Geophysicists, Tulsa, OK, 2017, pp. R1-1–R1-40.

[52] J. VIRIEUX AND S. OPERTO, *An overview of full-waveform inversion in exploration geophysics*, Geophysics, 74 (2009), pp. WCC1–WCC26.

[53] A. D. WHEELON, *Electromagnetic Scintillation*, Vol. 1, Cambridge University Press, Cambridge, 2001.

[54] A. D. WHEELON, *Electromagnetic Scintillation*, Vol. 2, Cambridge University Press, Cambridge, 2003.

[55] O. YU IMANUVILOV AND M. YAMAMOTO, *Global uniqueness and stability in determining coefficients of wave equations*, Comm. Partial Differential Equations, 26 (2001), pp. 1409–1425.

[56] C. ZHU, R. H. BYRD, P. LU, AND J. NOCEDAL, *Algorithm 778: L-BFGS-B: Fortran subroutines for large-scale bound-constrained optimization*, ACM Trans. Math. Software, 23 (1997), pp. 550–560.